Ocean Modelling 121 (2018) 1–18

Contents lists available at ScienceDirect

Ocean Modelling

journal homepage: www.elsevier.com/locate/ocemod

Eddy dynamics over continental slopes under retrograde winds: Insights from a model inter-comparison

Yan Wang*, Andrew L. Stewart

Department of Atmospheric and Oceanic Sciences, University of California, Los Angeles, CA 90095, USA

ARTICLE INFO

Keywords:
Mesoscale eddies
Continental slopes
Numerical ocean models
Eddy transfer
Eddy parameterization

ABSTRACT

Mesoscale eddies are ubiquitous in the ocean and play a key role in exchanges across continental slopes. In this study the properties of wind-driven baroclinic turbulence are investigated using eddy-resolving process simulations, focusing on the case of retrograde winds that arises around the margins of the subtropical gyres. In contrast to a flat-bottomed ocean, over steep slopes eddies develop from baroclinic instabilities are confined to the top few hundred meters. Deeper in the water column baroclinic instability and vertical momentum transfer are suppressed, so wind-input momentum is exported toward the open ocean by eddies before traversing down to the ocean bed. Close to the sloping topography, eddy energy sourced from the upper ocean is converted to potential energy, steepening isopycnals and driving bottom-trapped prograde flows. This process is associated with upgradient lateral buoyancy fluxes and downgradient isopycnal potential vorticity fluxes, and cannot be reproduced via linear stability calculations.

These properties of wind-driven shelf/slope turbulence are contrasted against simulations with flat bathymetry. The key differences described above hinge on the flow close to the steep topographic slope, which may be sensitive to the model's vertical coordinate system. The simulations are therefore replicated using models that employ geopotential coordinates, terrain-following coordinates, and isopycnal coordinates. Quantitative inter-model discrepancies in the momentum and energy budgets are much more pronounced in the presence of a steep bottom slope. However, the key findings of this study are consistent across the models, suggesting that they are robust and warrant incorporation into parameterizations of eddy transfer across continental slopes.

1. Introduction

Numerical ocean models are increasingly capable of resolving mesoscale eddies (*e.g.*, Maltrud and McClean, 2005). This parallels the growing observational evidence that oceanic eddies play a crucial role in modulating the large scale ocean circulation and long term climate evolution (Dong et al., 2014; Zhang et al., 2014). Eddies over continental slopes, in particular, are found to control the exchanges of heat, salt, and biogeochemical tracers between coastal and deep oceans, and subsequently impact water mass formations and global overturning (Spall, 2004; Pickart and Spall, 2007; Spall, 2010; Jungclaus and Mellor, 2000; Serra and Ambar, 2002; Thoma et al., 2008; Dinniman et al., 2011; Nøst et al., 2011; Hattermann et al., 2014; Stewart and Thompson, 2012; 2015b).

Eddy-induced transfer across continental slopes presents a challenge for ocean observing systems (Nencioli et al., 2016) in view of the fact that the local Rossby deformation radius may change sharply from tens of kilometers in the deep open ocean to only a few kilometers across the slope. This leads to an eddy field with a rich spectrum of variability (*e.g.*, Capet et al. 2008a,b,c) that is difficult to measure directly. Moreover, while dynamically significant cross-slope exchanges driven by eddies are weak and highly transient compared to the generally dominant alongshore flows. This renders measurement and isolation of eddy component from the mean field extremely challenging (Brink, 2016a,b).

Partly due to these observational limitations, eddy-resolving process model studies have been vital in facilitating the development and validation of parameterizations of eddy transfer for global ocean climate models (*e.g.* Visbeck et al., 1997). Most existing eddy parameterizations are implemented based on the local mean state of ocean and have only been validated against simulations of open-ocean eddies (Gent, 2011; Griffies et al., 2000b). Such parameterizations are unlikely to be applicable to continental slopes, which may introduce distinct turbulence regimes characterized by suppression of eddy transfer at depth and intensification near the surface (LaCasce, 1998; LaCasce and Brink, 2000). These dynamical distinctions must be incorporated into existing

* Corresponding author.
E-mail address: ywang@atmos.ucla.edu (Y. Wang).

https://doi.org/10.1016/j.ocemod.2017.11.006
Received 10 August 2017; Received in revised form 5 November 2017; Accepted 19 November 2017
Available online 21 November 2017
1463-5003/

eddy parameterizations to allow coarse-resolution global ocean models to accurately represent exchanges between continental shelves and the open ocean.

In order to simulate eddying flows accurately, models must use horizontal grids that can resolve at least the first Rossby radius of deformation (Hallberg, 2013) and vertical grids that can resolve one or more baroclinic modes (Stewart et al., 2017). In contrast, the influence of different vertical coordinate systems among various ocean models has received less emphasis. Each vertical coordinate system has its own merits and limitations in simulating oceanic flows (Chassignet et al., 2000; 2006; Willebrand et al., 2001). For instance (Griffies et al., 2000a), models employing the z-coordinate (*i.e.* geopotential levels) are effective in representing weakly stratified areas such as the surface mixed layer, whereas models using the isopycnal-coordinate (*i.e.* potential density surfaces) are more suitable for studying ocean interior tracer transport that is largely adiabatic (*i.e.* along isopycnal surfaces). In certain areas where steep topography produces leading order variations in ocean depth, σ-coordinate (*i.e.* terrain-following coordiante) models may be favorable.

In practice, different vertical coordinate systems may yield different results when applied to the same physical problem, regardless of how similarly the models are configured. A classic example of this issue is given by studies on density-driven overflows at high latitude, which consistently suggest that z-coordinate models, as compared with isopycnal- or σ-coordinate models, tend to generate excessive spurious diapycnal mixing as the dense water descends down the sloping bottom due to the staircase representation of bottom topography (Roberts et al., 1996; Ezer and Mellor, 2004; Legg et al., 2006). In the scenario of simulating the basin-scale dynamics of the North Atlantic, such flawed overflows lead to severe reduction of North Atlantic Deep Water formation and substantially weaken the Atlantic Meridional Overturning Circulation (Chassignet et al., 1996). Similarly, simulated baroclinic turbulence over continental slopes may be sensitive to the choice of vertical coordinate options and therefore model-dependent (Ezer, 2016).

In this study, we investigate wind-driven baroclinic turbulence over continental slopes and characterize its distinctions from the better understood case of turbulence over flat ocean bed (*e.g.* Visbeck et al., 1997; Abernathey et al., 2013). We have chosen to focus on flows driven by retrograde winds (*i.e.* winds directed counter to the direction of Kelvin wave propagation) for two reasons. First, linear stability theory suggests that prograde and retrograde flows exhibit qualitatively different responses to steepening of the bottom slope (Blumsack and Gierasch, 1972; Mechoso, 1980; Isachsen, 2011), and should therefore be addresses separately. Second, eddy transfer across prograde fronts has been shown to agree well with predictions by linear stability analysis (Spall, 2004; Pennel et al., 2012; Poulin et al., 2014), whereas eddy transfer across retrograde flows diverges substantially from linear predictions and warrants further investigation (Isachsen, 2011).

We conduct our simulations using the z-coordinate MIT general circulation model (MITgcm, Marshall et al., 1997), the σ-coordinate Regional Ocean Modeling System (ROMS, Shchepetkin and McWilliams, 2005), and the isopycnal coordinate Hallberg Isopycnal Model (HIM, Hallberg and Rhines, 1996). By using models that span the range of widely-used vertical coordinate systems, we are able to evaluate which of the diagnosed eddy behaviors are model-independent, and therefore dynamically robust. Furthermore, this approach serves as a tool for comparing the representations of flow-topography interactions in different ocean models. All three models have been documented in previous literature for studying eddy processes over continental regions: Stewart and Thompson (2015a) used the MITgcm to quantify shoreward eddy transport of Circumpolar Deep Water (CDW) across the Antarctic continental slope; similarly, Zhang et al. (2011) used HIM to examine the role of eddy-topography interactions in driving the cross-slope transport of CDW; Brink (2016a) and Brink and Seo (2016) uses ROMS to show that spatially uniform wind stress over a continental slope unconditionally creates ample potential energy (PE) to fuel baroclinic instabilities, independent of whether the forcing is upwelling-favorable, downwelling-favorable, or temporally oscillating.

In this manuscript we focus on the dynamics of baroclinic turbulence in a selected reference simulation, and on its representation across different models. Additional parameter sensitivity experiments, described briefly in Section 5, did not yield qualitatively different results. The rest of the article is organized as follows. In Section 2, we describe the model configurations used in this study. In Section 3 we characterize the properties of wind-driven baroclinic turbulence over continental slopes using our MITgcm reference simulation, as contrasted against simulations conducted with a flat ocean bed. In Section 4 we validate our findings via comparison with identical simulations conducted using ROMS and HIM, and quantify inter-model differences between the models' mean circulations, momentum/energy budgets and potential vorticity fluxes. Concluding remarks follow in Section 5.

2. Model configuration

In this section, we describe the models employed and the configuration of simulations. The values of physical parameters of our reference model runs are summarized in Table 1. To achieve an objective model inter-comparison, we have kept every aspect of the model configurations identical, where possible. Exceptions include the treatment of surface boundary layer, the prescription of biharmonic viscosity, and discretization schemes for momentum and tracer equations.

2.1. Model domain

We consider a zonally-uniform channel schematically illustrated in Fig. 1(a) with a continental shelf of 500 m depth located at the southern boundary of the domain. The shelf is deeper than most realistic continental shelves (*e.g.* Cacchione et al. 2002) to ensure that the flow field over the shelf and slope is adequately resolved in all models. The ocean is 4000 m deep at the northern boundary and shoals from the center of the domain toward the shelf across an idealized continental slope. Specifically, the bathymetry $z = h(y)$ is defined by

$$h(y) = -Z_s - \frac{1}{2}H_s \tanh\left(\frac{y - Y_s}{W_s}\right), \tag{1}$$

Table 1
List of parameters used in reference model runs.

	Value	Description
L_x	800 km	Zonal domain size
L_y	500 km	Meridional domain size
H	4000 m	Maximum ocean depth
Z_s	2250 m	Slope mid-depth
H_s	3500 m	Shelf height
Y_s	200 km	Mid-slope offshore position
W_s	50 km	Slope half-width
Y_w	200 km	Peak wind stress position
L_r	50 km	Width of northern relaxation
T_r	7 days	Northern relaxation timescale
τ_o	0.05 N m^{-2}	Wind stress maximum
L_w	400 km	Meridional wind stress width
ρ_0	1000 kg m^{-3}	Reference density
α	1×10^{-4} $^oC^{-1}$	Thermal expansion coefficient
g	9.81 m^2 s^{-1}	Gravitational constant
f_0	1×10^{-4} s^{-1}	Reference Coriolis parameter
β	4×10^{-11} m^{-1}s^{-1}	Planetary vorticity gradient for flat-bottomed runs
A_4^m	2.9×10^8 m^{4}s^{-1}	MITgcm biharmonic viscosity
A_4^h	5.8×10^8 m^{4}s^{-1}	HIM biharmonic viscosity
$\triangle x$	2 km	Horizontal grid spacing
$\triangle z$	10.5 m–103.8 m	Vertical level spacing (MITgcm)
$\triangle t$	131 s	Time step size

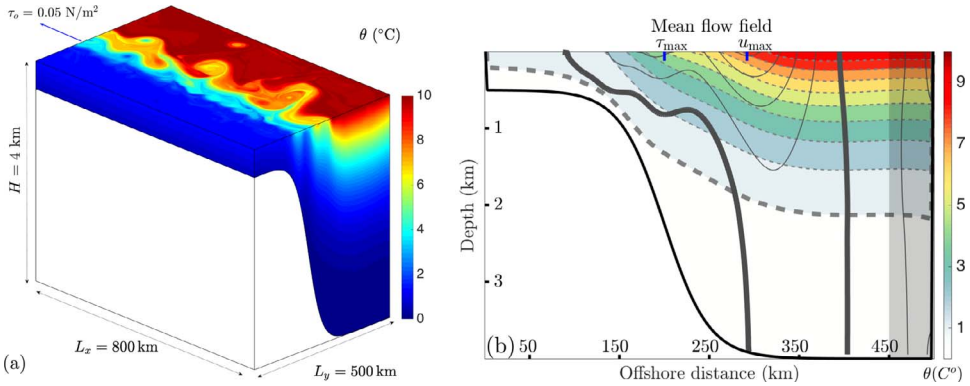

Fig. 1. (a) Model configuration. We simulate Boussinesq flow in a zonally-uniform, periodic channel on an $f-$plane with potential temperature restored to an exponential profile in a 50-km wide sponge layer at the northern boundary. Quadratic drag is imposed at bottom. The surface is forced by a retrograde wind stress whose maximum strength lies $y = 200$ km offshore, over the center of the slope. (b) Time-and-zonal mean stratification (colored dashed contours) and thermal shear current profiles (gray solid contours) derived from 5 years of statistically steady flow. The bold dashed contour denotes the $\theta = 1.0\ C^o$ isopycnal surface. The blue ticks at surface denote the locations of wind stress maximum and retrograde velocity maximum, the distance between which measures 92 km in latitude. The bold solid contour denotes $u = -0.1$ m/s. The shadowing at the northern boundary indicates the sponge layer. (For interpretation of the references to color in this figure legend, the reader is referred to the web version of this article.)

where y is the offshore distance (latitude), Z_s= 2250 m denotes the vertical slope position, H_s= 3500 m represents the shelf height, Y_s= 200 km marks the offshore slope position, and W_s= 50 km is the slope half-width. The channel spans 800 km and 500 km in the along-slope and cross-slope directions, respectively. Throughout this work we will use "along-slope" and "longitudinal" or "zonal" interachangeably, and similarly for the "cross-slope" with "latitudinal" or "meridional". The channel is posed on an f-plane because changes in depth dominate the background potential vorticity gradient, and so the slope can be thought of as being oriented in any direction relative to meridians. Similar configurations have been used for studying shelf/slope eddies and jets in the Southern Ocean using MITgcm (Stewart and Thompson, 2013; 2016; Stern et al., 2015).

A series of flat-bottomed runs are conducted with identical configurations of the slope runs except that the steep slope is replaced with a large planetary vorticity gradient $\beta = 4 \times 10^{-11}\text{m}^{-1}\text{s}^{-1}$ across the channel. The addition of an artificially large β is necessary for halting the indefinite growth of the energy-containing scale (Rhines, 1975; Maltrud and Vallis, 1991; 1992) without widening our domain. We found that simulations with no planetary vorticity gradient exhibited statistically steady states that were sensitive to their initial conditions.

2.2. Model grid and discretization

We use a horizontal grid spacing of 2 km in all model runs described here. Simulations conducted at higher (1 km) horizontal grid spacing yielded no qualitative differences from the results reported below. It should be noted that though all three models use the C-grid design and are set to be consistent in horizontal resolution, the algorithms for discretizing the momentum and tracer equations differ. Specifically, MITgcm adopts a finite volume scheme to solve the momentum equations in vector-invariant form and advects potential temperature using the second-order-moment scheme of Prather (1986). ROMS uses the third-order upwind advection scheme for both momentum and tracer equations. HIM employs the vorticity advection scheme of Arakawa and Hsu (1990) and advects isopycnal layer thicknesses using a positive-definite finite volume scheme.

Due to the differing vertical coordinate systems, it is difficult for models to achieve consistent vertical resolutions over a continental slope. We have therefore chosen to ensure matched resolutions in the open ocean by setting identical number of vertical levels to make as fair a comparison as possible. MITgcm runs are based on 70 vertical geopotential levels, with grid spacing increasing from 10 m at the surface to over 100 m at the ocean bed. Partial grid cells are used to improve resolution of flows over the continental slope (Griffies et al., 2000a). ROMS runs use 70 terrain-following vertical levels, with unequal vertical grid spacings that increase resolution close to the ocean bed and the sea floor. HIM runs employ 70 vertical isopycnal layers with thicknesses equal to the MITgcm geopotential grid cell thicknesses at the northern boundary. Where density surfaces outcrop or incrop, density layers may have non-zero but arbitrarily thin thicknesses (Hallberg and Rhines, 1996). Refining the vertical grids from 70 to 133 levels yields only slight quantitative changes in our results.

2.3. Forcing and boundary conditions

All model runs are forced at the surface by a steady alongshore wind stress with the profile defined by

$$\tau_x = -\tau_o \cdot \sin^2(y/L_w), \qquad 0 < y < L_w \tag{2}$$

where τ_o=0.05 N/m^2 denotes the maximum strength of wind located at the offshore slope position $Y_s = 200$ km, $L_w = 400$ km measures for the width of forcing in the offshore direction, and the negative sign on the right hand side of (2) corresponds to the retrograde (*i.e.* westward) direction of wind stress. No surface buoyancy flux is prescribed.

At the ocean bed, all model runs are subject to a drag stress with quadratic coefficient $C_d = 2.5 \times 10^{-3}$, serving as a sink for momentum and energy imparted by the surface wind stress.

Periodic boundary conditions are used in the alongshore direction. No-normal-flow conditions are imposed at the shoreward and offshore edges of the domain. The potential temperature (but not the velocity field) is restored to a reference exponential profile across a sponge layer of 50 km width at the northern boundary, with a maximum relaxation time scale of 7 days, to facilitate the evolution of ocean flow into a statistically steady state. This effectively fixes the first baroclinic Rossby deformation radius at approximately 18 km in the deep ocean. Expanding the channel width to 800 km while retaining identical relaxation at the northern boundary yielded negligible differences to the results.

2.4. Viscosity and mixing

The surface K-Profile Parameterization (KPP) (Large et al., 1994) is used in both MITgcm and ROMS with their respective default settings. The Richardson number dependent mixing parameterization is also turned on to simulate shear-driven diapycnal mixing. In HIM, we impose finite diffusivity and viscosity, both set to 5×10^{-3} m^2/s, over the upper 50 m of the water column. These values are chosen based on the surface mixed layer properties from the ROMS runs (determined by KPP) in statistically steady state.

In addition, an explicit biharmonic viscosity is used in both MITgcm and HIM runs for numerical stability. We found that a larger biharmonic viscosity was required in HIM (see Table 1) to suppress numerical instabilities at the southern wall. In ROMS runs the grid-scale energy, enstrophy, and tracer variance are controlled via the rotated-split third-order upwind advection scheme.

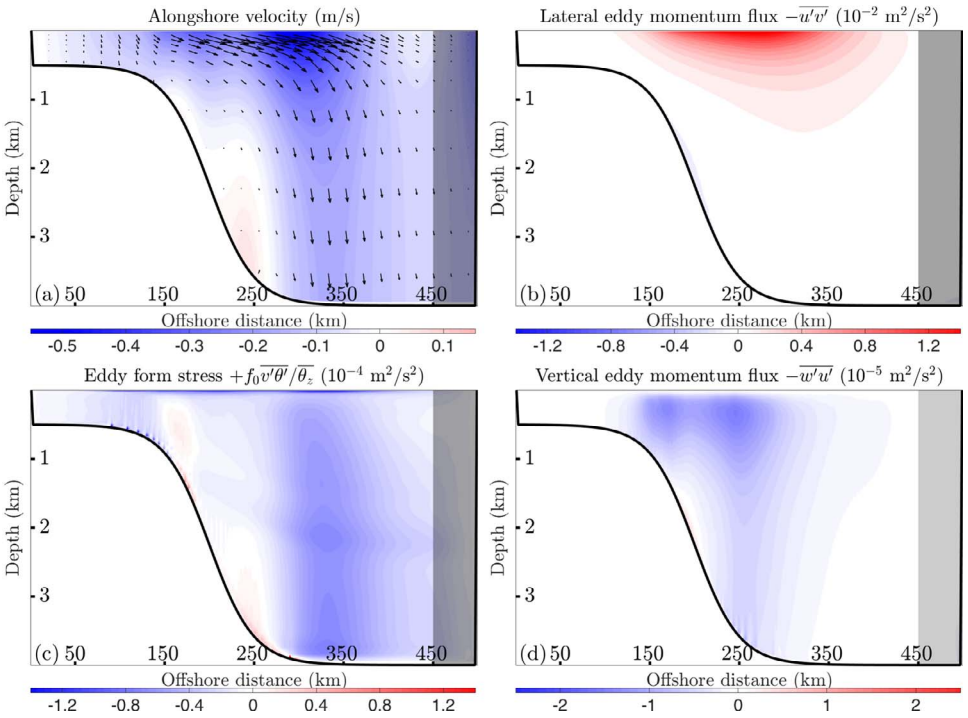

Fig. 2. Eddy transfer of along-shore momentum in our MITgcm shelf/slope reference simulation. (a) Eddy fluxes of retrograde momentum (arrows) overlaid upon mean along-slope current (colors). Blue (red) contours denote retrograde (prograde) flow, or flow into (out of) the page. (b) Horizontal eddy flux of retrograde momentum as a function of latitude and depth. Red (blue) contours denote offshore (onshore) flux of retrograde momentum. (c) Interfacial form stress as a function of latitude and depth. Blue (red) contours denote downward (upward) flux of retrograde momentum. (d) Vertical eddy flux of retrograde momentum as a function of latitude and depth with the same color convention in panel (c). All diagnostics are zonally and temporally averaged. The shadowing at the northern boundary indicates the sponge layer. (For interpretation of the references to color in this figure legend, the reader is referred to the web version of this article.)

2.5. Model integration

All models integrate the three-dimensional, hydrostatic Boussinesq momentum equations coupled with a linearized equation of state depending on potential temperature only.

Each simulation is spun up from a resting state at a coarse 4 km resolution for 35 years until a statistically steady state is reached, as determined from the time series of total kinetic energy and total potential temperature. The solutions are then interpolated onto a finer 2 km grid and re-run for another 15 years to re-establish statistical equilibrium. Daily fields taken from the final 5 years are used for analysis.

3. Continental slope eddy dynamics

In this section we describe the properties of baroclinic turbulence in our MITgcm shelf/slope reference run. Throughout this section we contrast our results against the better understood case of a flat-bottomed ocean (*e.g.* Visbeck et al., 1997; Abernathey et al., 2013). To simplify the presentation, we focus on the shelf/slope simulations, and include further information on the flat-bottomed simulation in Appendix B.

3.1. Stratification and thermal shear current

In statistically steady state, the surface wind stress has produced a retrograde front associated with a strong thermal shear current accompanied by an energetic eddy field throughout the channel (Fig. 1(a)). The structures of the time- and along-shore-mean stratification and thermal shear current are shown in Fig. 1(b). Two locations are highlighted with blue ticks at surface: one marks the latitude $y = Y_s = 200$ km where the wind stress is maximal, and the other indicates surface maximum of the thermal shear current. These two locations are separated by a distance of 92 km, indicating a pronounced asymmetry in the structure of the current relative to an otherwise symmetric surface wind stress profile. Furthermore, a closer inspection of the zonal velocity contours reveals that multiple zonal jets are embedded in the mean current, consistent with confinement of the energy-containing scale in the cross-shore direction by the topographic potential vorticity gradient (Rhines, 1975; Thompson, 2010). By contrast, in a flat-bottomed ocean the wind-driven current is almost perfectly symmetric about the wind stress maximum (see Appendix B).

3.2. Eddy momentum fluxes

In order to understand how the asymmetric current structure is established, we now analyze the momentum budget. Following Stewart and Thompson (2016), the time-and-zonal mean momentum equation is formulated as

$$\frac{\partial}{\partial t}\overline{u} + \frac{\partial}{\partial y}\overline{v'u'} + \frac{\partial}{\partial z}\left(\overline{w'u'} - f_0\frac{\overline{v'\theta'}}{\overline{\theta}_z}\right) \simeq f_0 v^{\dagger}, \tag{3}$$

under the Transformed Eulerian-Mean (TEM) framework (Plumb and Ferrari, 2005), where $\overline{\cdot}$ denotes the time and zonal mean operator at constant depths. Eq. (3) states that the divergence of eddy momentum fluxes per unit mass on the left-hand side are approximately balanced by the Coriolis acceleration resulting from the residual meridional flow $v^{\dagger}$ on the right-hand side. The time derivative term approximately vanishes after time averaging, but is retained here for clarity. The divergence of the mean momentum flux $\frac{\partial}{\partial y}(\overline{v}\cdot\overline{u}) + \frac{\partial}{\partial z}(\overline{w}\cdot\overline{u})$ is negligible in magnitude outside of thin surface and bottom boundary layers and thus omitted. Fluxes of along-slope momentum are then determined by the last three terms on the left hand side of (3), namely, the meridional eddy momentum flux $\overline{v'u'}$, the vertical eddy momentum flux $\overline{w'u'}$, and the eddy form stress $-f_0\frac{\overline{v'\theta'}}{\overline{\theta}_z}$, the geostrophic approximation of the vertical momentum transfer due to horizontal pressure gradient forces exerted against fluctuations of isopycnal interfaces (*e.g.* Vallis, 2006).

In Fig. 2(a), we indicate the direction and magnitude of the eddy momentum flux vector via arrows overlaid on the background thermal shear current. Here we have reversed the signs of the latter three terms in (3) to visualize the fluxes of *retrograde* momentum, and aid interpretation of their relationship to the retrograde winds and mean current. Note the almost lateral offshore eddy momentum flux confined in the top few hundred meters over the slope, and that downward transfer to the ocean bed occurs in the open ocean. Further notice that the

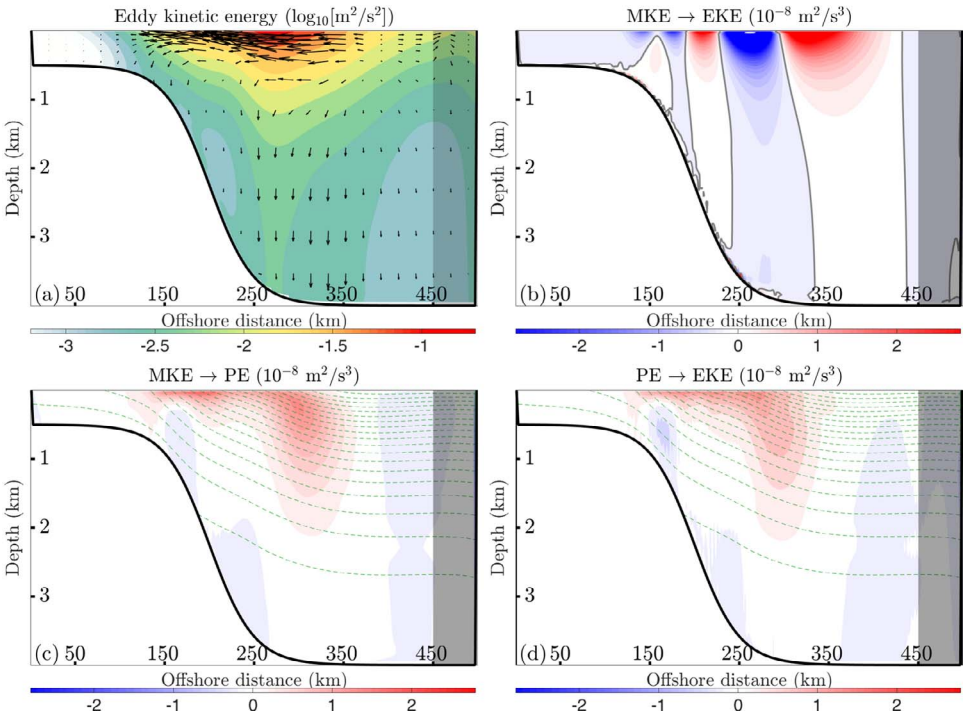

Fig. 3. Contributions to the eddy energy budget in our MITgcm shelf/slope reference simulation. (a) Logarithm of EKE (colored background contours) as function of latitude and depth with the net EKE flux vectors (arrows) imposed. (b) Conversion of MKE into EKE as a function of latitude and depth with zero conversions indicated by bold gray contours. (c) Conversion of MKE into PE as a function of latitude and depth with positive (negative) contour levels denoting PE gain (loss). (d) Conversion of PE into EKE as a function of latitude and depth with positive (negative) contour levels denoting EKE gain (loss). In all panels the sponge layer is shadowed at northern boundary. Green dashed contours in (c) and (d) indicate selected isopycnal surfaces.

overall eddy momentum flux pathway follows closely the structure of thermal shear current. The surface-confined lateral momentum flux appears to stem from above the center of the slope and extends as far as y= 400 km. This pattern of momentum transfer is consistent with suppression of eddy form stress close to the continental slope, requiring that surface-confined eddies instead export retrograde momentum toward the open ocean where full-depth baroclinic instabilties can transfer it to the ocean bed. The relocation of mean current via eddy momentum fluxes is similar to the adjustment of the structure of Agulhas Return Current by transient eddies in the Southern Ocean (Morrow et al., 1992).

Toward the sloping bottom, the thermal shear current weakens and turns prograde. This is evident near the junction to deep ocean and at the shelf break. Meanwhile, the local eddy momentum fluxes decrease sharply in magnitude. These processes are indicative of an isolated dynamical regime controlled by bottom topography. In Fig. 2(b) and (c) we plot the individual components of eddy fluxes of retrograde momentum. Note that lateral eddy momentum flux (Fig. 2(b)) is mainly confined over the upper few hundred meters and directed offshore. Over most of the domain, eddy form stress (Fig. 2(c)) dominates over the vertical eddy momentum flux (Fig. 2(d)) by approximately one order of magnitude. Approaching the slope, however, these two terms approximately compensate one another as the eddy form stress decreases rapidly in magnitude and even changes sign where there is a prograde thermal shear current (Fig. 2(a)), while the advective flux continues to transfer momentum downward.

3.3. Eddy kinetic energy budget

Though the interior eddy momentum budget clarifies how the structure of thermal shear current is determined, it does not offer information on means by which eddies are generated.

In classic quasi-geostrophic (QG) theory (*e.g.* Pedlosky 1987), eddies are generated via two mechanisms. One is baroclinic instability, in which potential energy feeds eddy growth. The other is barotropic instability, in which eddies extract kinetic energy from the mean flow. A necessary condition for baroclinic (barotropic) instability of a QG flow is that the background potential vorticity (PV) gradient should change sign in the vertical (cross-stream) direction. The reader is referred to Pedlosky (1987) and Vallis (2006) for a review and Isachsen (2011) for the interpretation of relevance of layer PV gradients to baroclinic instability. The presence of a sloping ocean bed may therefore alter the stability of a flow by modulating the background PV. For instance, early studies (Blumsack and Gierasch, 1972; Mechoso, 1980), based on the Eady (1949) model, predict that the ratio between the topographic slope and isopycnal slope, denoted by the slope parameter δ, determines the baroclinic stability of the along-slope flow. Our simulations correspond to the case $\delta > 1$, in which the ocean bed has the same inclination as, yet is more steeply tilted than, the isopycnals. Linear theory predicts that such flows should be stable, but the cross-slope eddy momentum flux discussed in the previous section indicates otherwise.

To identify the sources of eddies in our simulation, we formulate the interior EKE budget equation (*e.g.* Chang and Orlanski, 1993, Chapman et al., 2015 and Stewart and Thompson, 2016)

$$\frac{\partial}{\partial t}\frac{\overline{\mathbf{u}_h'^2}}{2} + \nabla\cdot\left(\overline{\mathbf{u}\cdot\frac{\mathbf{u}_h'^2}{2}} + \overline{\mathbf{u}'\phi'}\right) = -\overline{\mathbf{u}_h'\cdot(\mathbf{u}'\cdot\nabla)\overline{\mathbf{u}_h}} + \overline{w'b'}, \tag{4}$$

which states that in statistically steady state, the divergence of EKE fluxes per unit mass on the left hand side is approximately balanced by the production rates of EKE per unit mass from the reservoirs of MKE and PE on the right hand. Here $\mathbf{u}_h$ ($\mathbf{u}$) is the horizontal (total) velocity vector, $\phi = p/\rho_0$ denotes the hydrostatic pressure divided by the reference density, and $b = -(\rho - \rho_0)g/\rho_0$ represents the buoyancy. The local derivative term is retained here again for clarity. The EKE fluxes consist of two terms: $\overline{\mathbf{u}\cdot\frac{\mathbf{u}_h'^2}{2}}$ corresponds to the EKE flux driven by the total velocity field, and $\overline{\mathbf{u}'\phi'}$ denotes the EKE flux via eddy pressure work.

In Fig. 3(a), we plot the logarithm of the mean EKE per unit mass along with the net EKE flux vectors denoted by arrows. Note that EKE is intensified over the top few hundred meters yet almost depleted near the bottom slope around y = 200 km. The low EKE distribution near the slope is consistent with prior numerical studies asserting that steep slopes suppress eddy activities (Blumsack and Gierasch, 1972; Isachsen, 2011; Chen and Kamenkovich, 2013; Hetland, 2017). The surface

intensification over the slope along with the vertical penetration of EKE away in the open ocean suggest that these portions of the domain are dynamically decoupled from the region close to the sloping bottom, broadly consistent with the findings of LaCasce (1998) and LaCasce and Brink (2000). Moreover, EKE flux in the upper few hundred meters is directed onshore from the deep ocean, potentially serving as a non-local driver of eddy-mean flow interactions across the slope (*e.g.*Chen et al. 2014).

Fig. 3(b) shows the MKE/EKE conversion term $-\overline{\mathbf{u}_h'\cdot(\mathbf{u}'\cdot\nabla)\overline{\mathbf{u}}_h}$, with positive (negative) contour levels denoting EKE gain (loss) from (into) MKE. We can further expand this into four terms:

$$-\overline{\mathbf{u}_h'\cdot(\mathbf{u}'\cdot\nabla)\overline{\mathbf{u}}_h} = -\overline{v'u'}\frac{\partial}{\partial y}\overline{u} - \overline{v'v'}\frac{\partial}{\partial y}\overline{v} - \overline{w'u'}\frac{\partial}{\partial z}\overline{u} - \overline{w'v'}\frac{\partial}{\partial z}\overline{v}. \tag{5}$$

The first two terms quantify Reynolds stress work associated with eddy momentum fluxes acting parallel to the mean shear, characteristic of barotropic instabilities. The latter two terms quantify Reynolds stress work associated with vertical momentum fluxes and mean shear, *e.g.* as activated in Kelvin-Helmholtz instabilities (Brink, 2016a; Brink and Seo, 2016), which are parameterized via the Richardson number-dependent mixing in the KPP scheme. Calculation of these terms reveals that the total conversion on the left hand side of (5) is dominated by the first term on the right hand side, which is at least one order of magnitude larger than any of the remaining terms, suggesting that barotropic energy conversions in our model are primarily due to lateral eddy momentum fluxes and horizontal shear of the mean current. As surface-generated eddies propagate offshore, they convey retrograde momentum anomalies laterally (Fig. 3(b)), leading to alternating regions of convergence and divergence of momentum, effectively accelerating and decelerating different flanks of thermal shear zonal jets. These strong local barotropic sinks and sources of EKE largely compensate each other in a whole-domain integral. Contour levels of zero MKE/EKE conversion are plotted in Fig. 3(b) (gray bold lines) to elucidate the spacing of the three zonal jets identified in this simulation.

Though barotropic EKE production locally dominates the right-hand side of (4), Fig. 3(d) shows that in a domain-integrated sense, baroclinic production serves as the primary eddy energy source. However, in contrast to simulations conducted using a flat-bottomed ocean, the energy production is largely confined to the top few hundred meters over the slope. This agrees broadly with earlier studies on the suppressive influence of topography on baroclinic instabilities (Isachsen, 2011; Chen and Kamenkovich, 2013; Hetland, 2017). In addition, both the Rossby number of the mean flow (quantified by surface relative vorticity normalized by the Coriolis frequency) and the bulk Richardson number in the top 50 m of the water column approach $\mathcal{O}(1)$ over the slope (not shown), indicating that ageostrophic mixed layer instabilities may play a role in seeding eddies (Boccaletti et al., 2007; Fox-Kemper et al., 2008). Closer to the continental slope, EKE production weakens and becomes negative, with eddies giving up their energy to increase PE. Such a conversion of EKE into PE is unexpected, because the tilted isopycnals (see green dashed contours in Fig. 3(d)) indicate an abundance of available potential energy. It then follows that EKE close to the slope must be sourced non-locally (*e.g.* Chen et al. 2014), consistent with the surface-confined shoreward EKE flux (Fig. 3(a)).

As PE is the ultimate source of the eddy energy, in Fig. 3(c) we plot the MKE to PE conversion rate per unit mass, $\psi_{\text{mean}}\frac{\partial \bar{b}}{\partial y}$ (Stewart and Thompson, 2016), where ψ_{mean} denotes the mean overturning streamfunction induced by Ekman transport. The PE production is largely the result of wind-driven Ekman pumping and suction, which creates vertical mean flows that serve to tilt isopycnal surfaces. Similar to the baroclinic EKE production, the PE production is confined close to the surface over the continental slope. Regions of PE destruction are found close to the ocean bed over the slope, indicating that vertical mean flows are acting to reduce isopycnal slopes and thereby remove the potential energy being created by eddies (see Fig. 3(d)).

3.4. Ageostrophic circulation

The presence of prograde jets associated with the conversion of EKE into PE attached to the sloping bottom suggests a locally distinct ageostrophic flow field compared to that in the deep ocean and the flat-bottomed ocean (*c.f.* Appendix B). We therefore now examine the isopycnal, mean, and eddy overturning streamfunctions, defined as (*e.g.* Wolfe and Cessi 2009)

$$\psi_{\text{iso}}(y,z) \equiv \Psi_{\text{iso}}(\hat{y},\hat{\theta}) = \overline{\int_{-H}^{0} v\cdot\mathscr{H}(\theta-\hat{\theta})dz}, \tag{6a}$$

$$\psi_{\text{mean}}(y,z) \equiv \Psi_{\text{mean}}(\hat{y},\hat{\theta}) = \frac{1}{L_x}\oint\int_{-H}^{0}\langle v\rangle\cdot\mathscr{H}(\langle\theta\rangle-\hat{\theta})dzdx, \tag{6b}$$

$$\psi_{\text{eddy}} = \psi_{\text{iso}} - \psi_{\text{mean}}, \tag{6c}$$

respectively. Here $\langle\cdot\rangle$ denotes a 5-year-long time-mean operator at constant depths, $\mathscr{H}$ is the Heaviside step function, and $(\hat{y},\hat{\theta})$ refer to the potential temperature coordinates following the convention of Wolfe (2014). The isopycnal and residual streamfunctions are defined in potential temperature coordinates, but mapped back to geopotential coordinates for presentation purposes using the time-/zonal-mean potential temperature field at each latitude.

We plot $\psi_{\text{mean}}(y,z)$ and $\psi_{\text{eddy}}(y,z)$ in Fig. 4(a) and (b), respectively. In the open ocean, surface and bottom Ekman transport imposes a clockwise cell in ψ_{mean} occupying the full water depth, whereas ψ_{eddy} exhibits a counterclockwise circulation with similar strength as ψ_{mean}. Approaching the sloping bottom, both ψ_{mean} and ψ_{eddy} exhibit sharp transitions. In particular, ψ_{mean} exhbits counterclockwise cells at the shelf break and near the junction to deep ocean, whereas ψ_{eddy} exhibits clockwise cells around the same locations. The approximate compensation across the channel between ψ_{mean} and ψ_{eddy}, resembling that in the Antarctic Circumpolar Current (Marshall and Radko, 2003), is due to the absence of surface buoyancy forcing, and is evident in the much weaker isopycnal overturning streamfunction shown in Fig. 4(c) – (d).

A clockwise (counterclockwise) cell in ψ_{eddy} near (away from) the slope suggests locally upgradient (downgradient) eddy buoyancy fluxes. Effectively, isopycnal surfaces near the slope are tilted up by eddies that ultimately reverse the thermal shear current by enhancing the meridional buoyancy gradient, while feeding the local pool of PE by consuming EKE, whereas eddies away from the slope act to flatten the sloping isopycnals converting PE into EKE. The latter process is triggered by baroclinic instabilities that penetrate throughout the water column in the deep ocean (Fig. 3(d)), while the former can only be sustained by non-local sources of EKE (Fig. 3(b)-d)). In parallel, the counterclockwise rotation of ψ_{mean} is supported dynamically by the divergence of eddy retrograde momentum fluxes, in addition to bottom friction. To see this, we note that $\psi_{\text{eddy}} \simeq \frac{\overline{v'\theta'}}{\bar{\theta}_z}$ under the TEM framework (Marshall and Radko, 2003; Plumb and Ferrari, 2005; Vallis, 2006) and re-cast (3) as

$$\frac{\partial}{\partial t}\overline{u} + \frac{\partial}{\partial y}\overline{v'u'} + \frac{\partial}{\partial z}\overline{w'u'} \simeq f_0\bar{v}. \tag{7}$$

Because the time derivative term in (7) is negligible in statistically steady state, the negative $\bar{v}$ associated with a counterclockwise ψ_{mean} cell near the slope requires divergent eddy fluxes of retrograde momentum, consistent with the momentum pathway shown in Fig. 2(a).

The residual overturning streamfunction $\Psi_{\text{iso}}(\hat{y},\hat{\theta})$ and its projection in the Cartesian space $\psi_{\text{iso}}(y,z)$ exhibit much weaker strength compared to ψ_{mean} and ψ_{eddy}. In particular, the maximum value of $\psi_{\text{iso}}(y,z)$ is approximately 15% of the total Ekman transport. In the absence of surface buoyancy forcing, the isopycnal overturning circulation $\psi_{\text{iso}}(y,z)$ is driven primarily by eddy stirring of buoyancy along the ocean surface and the bottom slope. This mixing might be enhanced by the "staircase" representation of topography in MITgcm (Hill et al.,

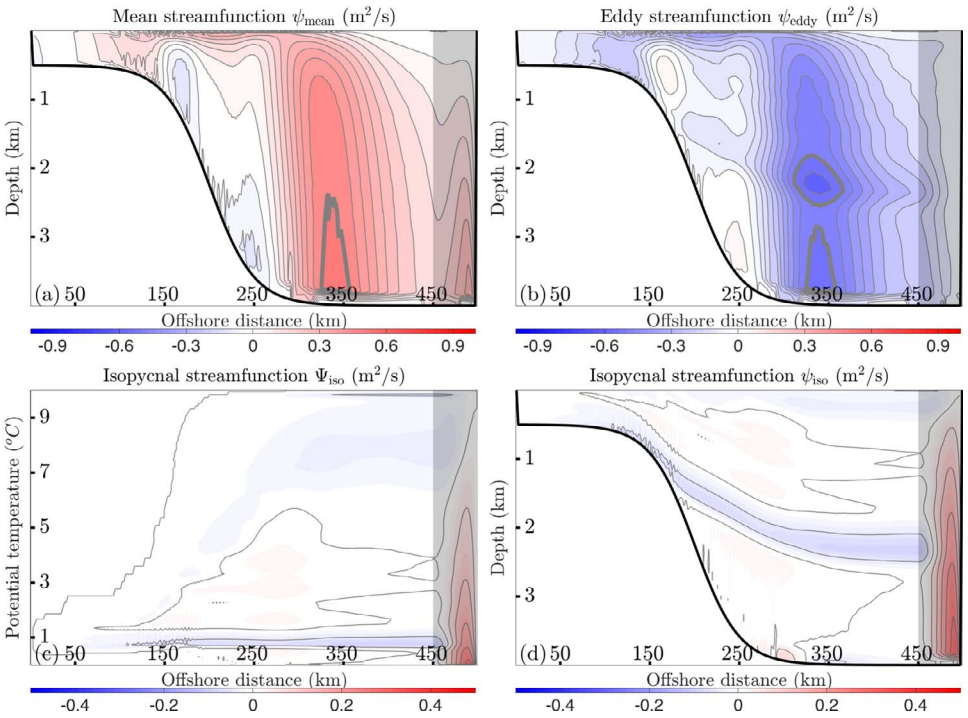

Fig. 4. Ageostropic circulation in our MITgcm shelf/slope reference simulation. (a) Mean overturning streamfunction in latitude/depth plane. Positive (negative) contours denote clockwise (counter-clockwise) rotation. The gray contour indicates the 0.5 m^2/s streamline. (b) Eddy overturning streamfunction in latitude/depth plane. The gray contour indicates the -0.5 m^2/s streamline. (c) Isopycnal overturning streamfunction in latitude/potential temperature space. (d) Isopycnal overturning streamfunction in latitude/depth space. The northern sponge layer is shadowed in all panels.

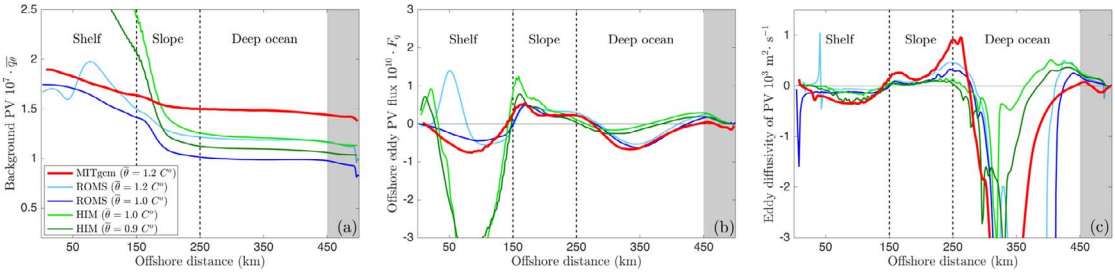

Fig. 5. (a) Mean potential vorticity along selected isopycnal surfaces as functions of latitude for the slope runs of MITgcm (green), ROMS (blue), and HIM (green). (b) Zonal-mean offshore eddy potential vorticity fluxes as functions of latitude on the same isopycnal surfaces as in panel (a). (c) Zonal-mean isopycnal eddy diffusivity for potential vorticity as a function of latitude along the same isopycnal surfaces as in panel (a) and (b). In all panels the northern sponge layer is shadowed. (For interpretation of the references to color in this figure legend, the reader is referred to the web version of this article.)

2012; Griffies et al., 2000a,b), and partly motivates our reproduction of this simulation setup in ROMS and HIM.

3.5. Generation of slope-trapped flows

One physical interpretation of the existence of slope-trapped flows accompanied by PE production from EKE is that eddies over the slope transfer PV downgradient to destroy mean potential enstrophy, and in doing so transfer their energy to the mean flow (see Bretherton and Haidvogel, 1976; Salmon, 1998; Marshalll et al., 2012). From the perspective of statistical mechanics, maximizing the entropy of the physical system while conserving energy and potential enstrophy gives rise to prograde mean flows (Holloway, 1978; 1986; 1992; 1993), and is referred to as the "Neptune effect" (Holloway, 1996). This entropy maximization is equivalent to minimizing the potential enstrophy associated with the mean flow in the "low-energy limit" (Venaille, 2012; Venaille et al., 2012).

Here we provide a qualitative assessment on this conjecture by analyzing the meridional eddy PV flux. The PV, the eddy component of its meridional flux, and the PV diffusivity are calculated via

$$q = (f_0\hat{\boldsymbol{z}} + \nabla \times u)\cdot\nabla\theta, \tag{8a}$$

$$F_q = \frac{1}{L_x}\oint_{\langle\theta\rangle} \mathrm{d}x\, \langle \boldsymbol{u}'q'\rangle\cdot\hat{\boldsymbol{s}} \tag{8b}$$

$$\kappa_\theta = \frac{1}{L_x}\oint_{\langle\theta\rangle} \mathrm{d}x\, \frac{\langle \boldsymbol{u}'q'\rangle\cdot\hat{\boldsymbol{s}}}{[\partial q/\partial y]_{\langle\theta\rangle}} \tag{8c}$$

where $\hat{\boldsymbol{z}}$ is the vertical unit vector and $\hat{\boldsymbol{s}} = \nabla\langle\theta\rangle/|\nabla\langle\theta\rangle| \times \hat{\boldsymbol{x}}$ is a unit vector parallel to time-mean potential temperature surfaces, $\hat{\boldsymbol{x}}$ is the zonal unit vector. The subscript $_{\langle\theta\rangle}$ denotes quantities evaluated at constant time-mean potential temperature $\langle\theta\rangle = 1.2\ ^oC$, which spans the meridional width of the channel without outcropping or incropping. Calculations based on nearby surfaces such as $\langle\theta\rangle = 1.0\ ^oC$ do not yield qualitatively different results. Note that (8a) and (8b) is an approximation to the eddy potential vorticity flux defined relative to the thickness-weighted average velocity and PV fields (*e.g.* Abernathey et al. 2013). These formulations of the eddy PV flux are formally identical in the limit of small isopycnal height fluctuations.

The mean PV and the zonal-mean eddy PV flux are plotted with red curves in Fig. 5(a) and (b), respectively. Background PV gradient is oriented onshore throughout the channel, *i.e.* $[\partial q/\partial y]_{\langle\theta\rangle} < 0$, due to the dominant role of planetary vortex stretching. In contrast, eddy PV flux appears to be upgradient (*i.e.* onshore) in the deep ocean yet downgradient (*i.e.* offshore) over the slope. The global maximum lies near the

Table 2
List of chosen diagnostics outside of sponge layers extracted from the slope model runs. All values are zonally and temporally averaged.

	MITgcm	ROMS	HIM
Retrograde velocity maximum (m/s)	0.52	0.44	0.66
Net retrograde transport (Sv)	132	147	120
Baroclinic retrograde transport (Sv)	56	62	63
Barotropic retrograde transport (Sv)	76	85	57
Wind stress maximum–retrograde velocity maximum offset (km)	92	99	72
Prograde velocity maximum (cm/s)	6.04	6.03	3.10
Depth of prograde velocity maximum (km)	3.33	1.45	1.66
Total EKE across channel (10^6 GJ)	7.20	7.23	3.19
PE → EKE conversion over slope (GJ/s)	0.31	0.20	0.17
PE → EKE conversion over slope (top 300m) (GJ/s)	0.17	0.14	0.11
EKE → PE conversion over slope (GJ/s)	0.04	0.15	0.04
Net MKE → EKE conversion (GJ/s)	0.052	−0.139	−0.168
Net PE → EKE conversion (GJ/s)	1.285	0.980	0.720

shelf break, coinciding with prograde flow along the ocean bed and production of PE at the expense of EKE. Fig. 5(c) shows the eddy diffusivity κ_θ, which is positive (downgradient) and $\mathcal{O}(100\text{–}1000\,\mathrm{m^2/s})$ across the slope, but then turns sharply negative (upgradient) in the deep ocean, with magnitudes typically far exceeding $1000\,\mathrm{m^2/s}$.

We now employ an approximate QG formulation to relate this pattern of PV mixing to the momentum and energy budgets. Formally, the $\mathcal{O}(1)$ change in ocean depth and isopycnal layer thicknesses put our simulations beyond the validity of the QG approximation, but QG carries the advantage of relative simplicity and thus ease of interpretation, and often facilitates understanding of eddy mixing processes in non-QG systems (*e.g.* Abernathey et al. 2013). We rewrite (3) as

$$\frac{\partial}{\partial t}\overline{u} = \overline{v' q'_{QG}} + f_0 v^\dagger, \tag{9}$$

where

$$\begin{aligned}\overline{v' q'_{QG}} &= -\frac{\partial}{\partial y}\overline{v'u'} - \frac{\partial}{\partial z}\overline{w'u'} + f_0 \frac{\partial}{\partial z}\left(\frac{\overline{v'\theta'}}{\overline{\theta}_z}\right) \\ &\simeq -\overline{\frac{\partial}{\partial y}\bigg|_\theta v'u'} + f_0 \frac{\partial}{\partial z}\psi_{\mathrm{eddy}}.\end{aligned} \tag{10}$$

Here we have retained the QG assumption of small isopycnal layer thickness variations and fluctuations, but relaxed the QG assumption of small isopycnal slope. Our formulation therefore differs from the usual QG PV flux (*e.g.* Vallis, 2006) via the inclusion of the vertical momentum flux divergence $\frac{\partial}{\partial z}\overline{w'u'}$. This term is non-negligible because lateral momentum transfer is largely aligned with isopycnals, which are steeply tilted over the continental slope. Further note that the Reynolds stress term $\partial_y \overline{u'v'}$ is often neglected altogether based on small Rossby number arguments (*e.g.* Abernathey et al., 2013), but is retained here because it plays a leading role in the momentum budget.

Eq. (9) implies that in statistically steady state, an offshore eddy PV flux must be balanced by a shoreward isopycnal transport $v\dagger < 0$. Fig. 4 shows that this transport occurs via a pair of weak positive and negative overturning cells over the slope, closed diabatically at the ocean surface, over the sloping ocean bed, and in the northern sponge layer. In the upper part of the water column at the shelf break ($y \approx 160\,\mathrm{km}$, $z \approx -250\,\mathrm{m}$) the eddy streamfunction increases with depth (Fig. 4(b)), corresponding to an upgradient eddy thickness flux and an upgradient contribution to the PV flux (10). However, this upgradient contribution is opposed by a stronger downgradient contribution due to Reynolds stress divergence associated with the strong offshore flux of retrograde momentum (Fig. 2(b)). Deeper in the water column at the same latitude ($y \approx 160\,\mathrm{km}$, $z \approx -800\,\mathrm{m}$), the Reynolds stress divergence weakens but eddy streamfunction gradient changes sign, resulting in downgradient fluxes of both thickness and PV. Here the isopycnals are strongly tilted, so this downgradient thickness flux actually corresponds to a buoyancy flux directed downward and offshore (laterally upgradient), and so produces PE at the expense of EKE.

The near-slope consumption of EKE and destruction of mean potential enstrophy via the downgradient eddy PV flux are qualitatively consistent with the "Neptune effect" (Holloway, 1992). However, these features do not appear consistently across the continental slope, but are rather confined to two prograde jets, visible in Fig. 2(a). This is in agreement with previous studies of statistical mechanics of turbulence over topographic slopes (Vallis and Maltrud, 1993; Venaille, 2012). In practice, cross-slope eddy PV mixing is approximately confined by the topographic Rhines scale, and the realized equilibrium state does not reach the theoretical maximum entropy state of the system in which prograde flows occupy the entire slope.

4. Model inter-comparison

Our PV mixing analysis indicates a distinct flow regime near the slope. However, it remains unclear whether these near-slope flows are being correctly simulated, particularly given the "staircase" representation of topography in MITgcm and the appearance of a non-negligible isopycnal overturning circulation despite the absence of surface buoyancy forcing (Fig. 4(d). As outlined in Section 2, this motivated us to recreate the simulation setup as closely as possible using ROMS and HIM, spanning the range of widely-used model vertical coordinate systems.

In general, all three models produce qualitatively similar results to those described in Section 3. In this section we therefore primarily focus on quantitative differences between the models. In Table 2 we quantify various properties of the statistically steady state over shelf/slope topography in all three models. To ensure an accurate comparison, daily snapshots of velocity and potential temperature from HIM were interpolated to geopotential coordinates before calculating all results discussed below.

4.1. Total momentum budget

In statistically steady state, each model exhibits an upwelling front with a mean retrograde thermal shear current over most of the domain (similar to Fig. 1). Here we choose to focus on three aspects of the mean current, namely, the strength of thermal shear exhibited by the magnitudes of surface/bottom velocity profiles, the cross-slope offset of surface current maximum from the wind stress maximum location, and the manifestation of the prograde jets attached to the slope.

The mean surface (u_{surf}) and bottom (u_{bot}) zonal velocity profiles are plotted in Fig. 6(a). Both ROMS and HIM exhibit qualitatively similar thermal shear currents to MITgcm. In particular, their surface retrograde flow maxima are shifted offshore from the slope, there are cross-slope oscillations of u_{surf} associated with multiple retrograde zonal jets, and prograde jets form at the ocean bed over the slope. These findings suggest that the asymmetric mean current structure and the topographically controlled flow field in the MITgcm run are not qualitatively model-dependent.

Despite the nearly identical configurations of the three models, surprisingly large quantitative differences arise between them. The deviation of the surface current core is 7 km larger in ROMS and 20 km smaller in HIM than that in MITgcm (see Table 2 and the circled dot markers in Fig. 6). Whereas the MITgcm and ROMS simulations exhibit three distinct surface retrograde jet cores, the HIM simulation only exhibits two.[1] In addition, the surface retrograde flow in ROMS has a smaller global maximum but extends further offshore, implying that on

[1] The jets exhibit pronounced variability, especially those at the surface over the slope (not shown). However, over the five-year average used in this study the jets are robust features: computing the mean velocities from different 5-year periods in the same simulation yields much smaller changes in the jet structure than the magnitudes of the inter-model differences in the jets.

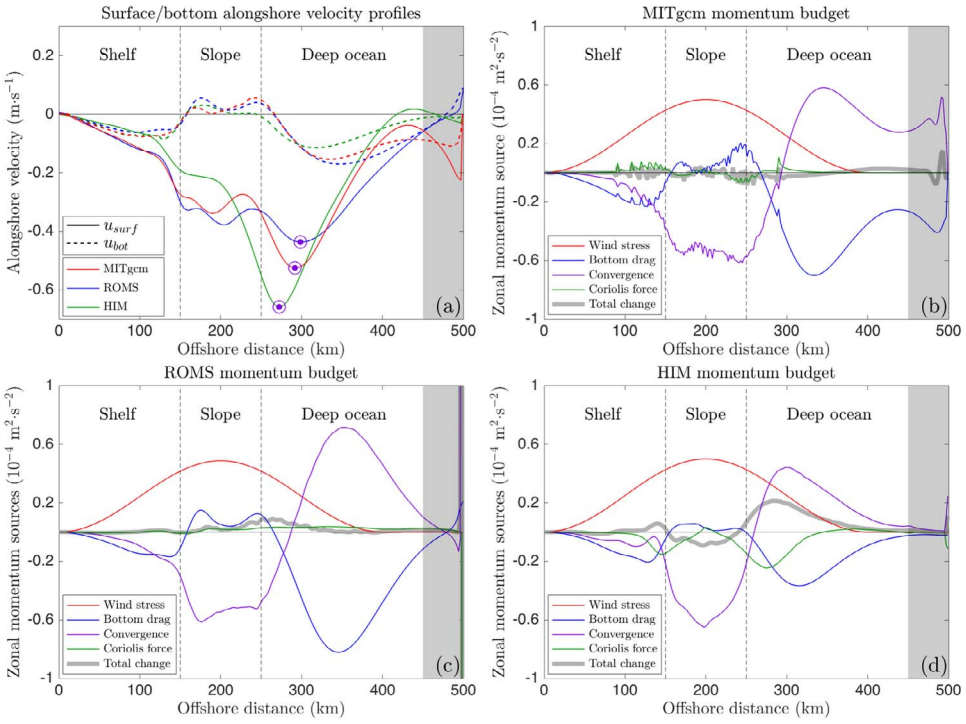

Fig. 6. Comparison of model momentum budgets. (a) Time- and zonal-mean surface (solid) and bottom (dashed) along-slope velocity profiles as functions of latitude produced by MITgcm (red), ROMS (blue), and HIM (green) in statistically steady state. Global extrema of surface velocity are marked by purple dots. (b–d) Depth-integrated momentum budget terms for (b) MITgcm, (c) ROMS, and (d) HIM. Total rates of change in momentum are plotted as bold gray curves; red curves indicate the input rate of momentum by surface wind stress; blue curves indicate the momentum extraction rate via bottom drag; purple curves indicate advective momentum convergence; green curves indicate the Coriolis acceleration exerted due to the depth-integrated meridional flow. The northern sponge layer is shadowed in all panels. (For interpretation of the references to color in this figure legend, the reader is referred to the web version of this article.)

average retrograde momentum in ROMS is exported further from the location of wind stress maximum by eddies than it is in MITgcm. On the other hand, HIM generates the strongest surface current over three models, and this flow is confined closer to the continental slope, where isopycnals tend to be more steeply tilted and thus the baroclinicity is larger. HIM therefore exhibits a slightly stronger baroclinic along-slope transport, but a much weaker barotropic along-slope transport than those found in the MITgcm and ROMS simulations (Table 2).

Although some effects of different vertical coordinate systems on representing the mean current can be understood by analyzing Fig. 6(a), the momentum balance provides greater insight. We formulate the vertically-integrated mean momentum budget as

$$\frac{\partial}{\partial t}\overline{U} + \frac{\partial}{\partial y}\overline{V^*U} - f_0\overline{V} = \frac{\tau_x}{\rho_0} - C_d\overline{(u_{\mathrm{bot}}^2 + v_{\mathrm{bot}}^2)^{\frac{1}{2}}u_{\mathrm{bot}}}, \tag{11}$$

where $\overline{U}$, $\overline{V}$, and $\overline{V^*U}$ are the vertical integrals of $\bar{u}$, $\bar{v}$, and $\overline{vu}$, respectively. Notice that (11) is just the vertical integral of (7) plus the source/sink terms due to surface/bottom stresses, and differs from the vector-invariant form of the momentum equation that is used to integrate the models. Eq. (11) states that the rate of change in the mean zonal momentum is determined by four factors in order, namely, the lateral divergence of retrograde momentum flux, the Coriolis force induced by mean meridional flow,[2] the wind stress, and the bottom drag. We plot these terms as functions of latitude in Fig. 6(b)–(d) for MITgcm, ROMS, and HIM.

In general, the models exhibit qualitative consistency in their momentum budgets. In particular, momentum imparted by surface wind stress over the slope is balanced by horizontal momentum flux divergence. A corresponding offshore momentum flux convergence leads the offshore deviation of thermal shear current (Fig. 6(a)). Over the slope the bottom drag actually serves as a source of retrograde momentum, and thereby removes momentum from the prograde jets attached to the slope. In the deep ocean, surface momentum input by wind is everywhere small compared to its extraction by bottom drag.

It is instructive to examine how this momentum balance changes in the absence of the continental slope. Fig. 7(a) shows identical diagnostics as in Fig. 6(b)–(d), but calculated from flat-bottomed simulations of each of the three models. For clarity, the shelf, slope, and deep ocean regions in the slope runs are now referred to as South, Core, and North regions, respectively. In this case the models are both qualitatively and quantitatively similar: momentum injected by wind is largely transfered directly downward and removed by bottom drag, with a modest convergence of momentum in the Core region by eddies. This is consistent with previous studies of wind-driven channel flows on a β-plane (*e.g.* Marshall and Radko, 2003; Abernathey et al., 2013), but qualitatively different from the shelf/slope in which eddies transfer all of the wind-input momentum offshore. The close quantitative agreement between the models in the flat-bottomed case suggests that the more substantial quantitative differences in the shelf/slope case stem from their differing representations of flow over topography.

In the shelf/slope simulations we identify four major quantitative inter-model discrepancies: First, in contrast with MITgcm, the ROMS and HIM momentum budgets show higher drag at the top of the slope than at the bottom, accompanying stronger prograde slope-trapped jets at the top of the slope. Second, the latitudinal spikes over the slope in the MITgcm momentum budget terms (Fig. 6(b)) are similar to those found by Ezer (2016) in a depth-integrated vorticity budget analysis, and are due to the "staircase" representation of topography. Third, in the deep ocean, momentum flux convergence is strongest in ROMS and weakest in HIM, yet the maximum along-slope velocity is largest in HIM and weakest in ROMS. This counter-intuitive result occurs because stronger momentum fluxes also push the momentum further from the topographic slope, where baroclinicity is weaker, thus ROMS also has the strongest barotropic component in its along-slope transport and HIM the weakest (see Table 2). Fourth, while both MITgcm and ROMS show negligible residual terms in their momentum budgets, HIM's residual is comparable to the magnitude of the wind stress. This is true even when computed using online averages of terms in the momentum equation (see Appendix A), and when the large spurious Coriolis force term is accounted for. The flat-bottomed HIM simulation does not produce a comparable residual in the momentum budget, (Fig. 7(a)),

[2] Physically, the depth-integrated Coriolis term necessarily vanishes because the flow is incompressible and f_0 is a constant. However, this term makes a non-zero contribution to the model momentum budgets due to the ways the Coriolis forcing are discretized in the three models.

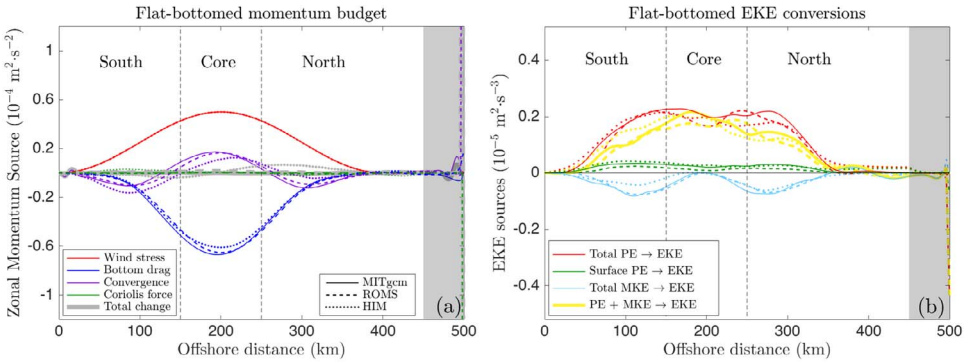

Fig. 7. Momentum and energy budgets from flat-bottom simulations. (a) Depth-integrated momentum budget terms as functions of latitude for MITgcm (solid line), ROMS (dashed line), and HIM (dotted line). The channel is divided arbitrarily into South, Core, and North regions, paralleling the Shelf, Slope and Deep ocean regions defined for the shelf/slope runs. (b) Depth-integrated EKE budget terms runs as functions of latitude using the same line type convention as (a). The northern sponge layer is shadowed in both panels.

suggesting that outcropping of isopycnals surfaces in the presence of a steep slope introduces substantial errors in HIM's momentum balance.

4.2. Energy budget

Fig. 8(a) shows the structures and magnitudes of depth-integrated EKE over the full water columns and upper 300 m. There is qualitative consistency in the EKE profiles between models in that they are approximately symmetric around the EKE maxima, which are displaced offshore of the continental slope. In addition, 40–50% of the EKE in the Slope region is concentrated within the top 300 m of the water column. Quantitatively, MITgcm and ROMS produce indistinguishable EKE profiles, and have more than twice as much domain-integrated EKE as HIM (Table 2).

In Fig. 8(b)–(d), we present the conversions of PE and MKE into EKE integrated over the total depths and top 300 m for each of the three models. Over the slope, baroclinic instabilities are surface intensified with approximately 60% of total production of EKE from PE confined within the uppermost 300 m (Table 2), which may partly hinge on surface mixed layer instabilities (Boccaletti et al., 2007; Fox-Kemper et al., 2008). In the deep ocean the near-surface EKE production is similar to that over the slope, but sub-surface baroclinic instabilities are no longer suppressed by topography, so EKE production substantially increases. The negative baroclinic EKE production at the shelf break ($y \approx 170$ km) is due to sub-surface EKE consumption and PE production, which is largest in ROMS and smallest in HIM in order (Table 2). Reynolds stress work (MKE → EKE) is largely confined to the uppermost 300 m of the water column and oscillates with latitude in all three models, highlighting the presence of multiple retrograde jets. The mixed barotropic-baroclinic instabilities associated with these jets seem contradictory with the findings by Killworth (1980), who asserts that a jet flow is dominated by baroclinic (barotropic) instabilities if its spatial scale is much larger (smaller) than the local deformation radius. Yet barotropic energy conversion in our simulations is essentially a response of baroclinic eddies to the steep slope that suppresses the vertical transfer of momentum. Consequently, though the total EKE production/consumption at each latitude is locally dominated by Reynolds stress work, the domain-integrated effect of this term is small in all three models.

Fig. 7(b) shows that when the continental slope is removed, baroclinic instabilities become the only EKE source throughout the channel (see also Appendix B). Note that the maximal baroclinic conversion rates in the flat-bottom cases (Fig. 7(b)) are one order of magnitude smaller than those in the shelf/slope cases (Fig. 8(b)–(d)). In addition, the top 300 m now capture only about 10% of the total baroclinic EKE production in the Core region, suggesting that the continental slope confines baroclinic instabilities to near-surface waters. Reynols stress work is a weak EKE sink in the vicinity of wind stress maximum (*c.f.*

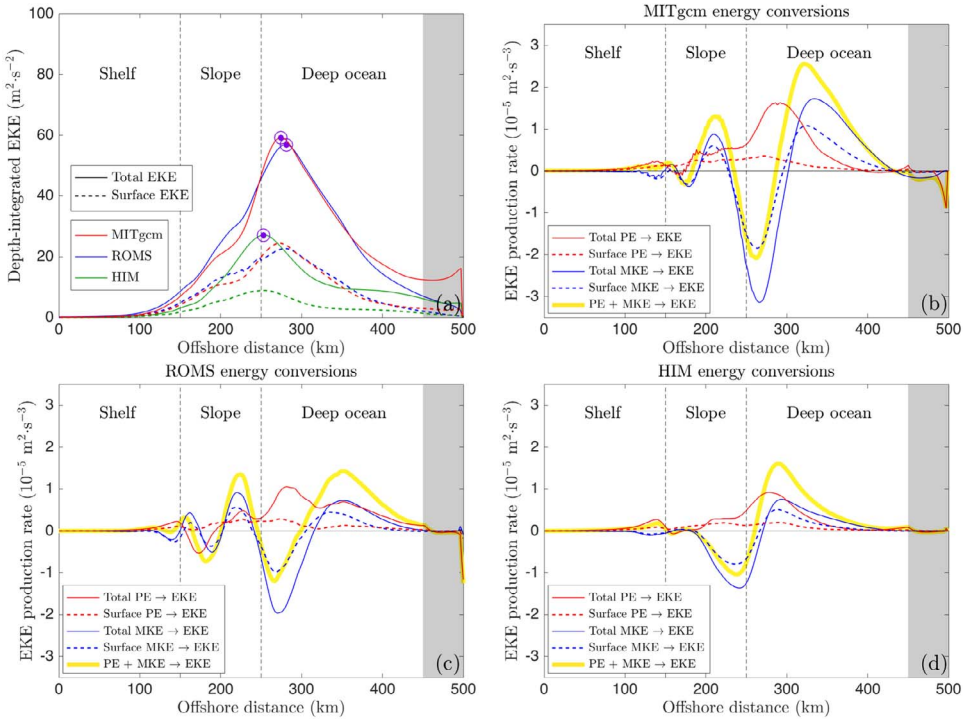

Fig. 8. Comparison between model eddy energy budgets. (a) Depth-integrated EKE profiles as functions of latitude with maximal values marked by circled dots for MITgcm (red), ROMS (blue) and HIM (green). Panels (b)–(d) show various energy conversion terms in MITgcm, ROMS, and HIM, respectively. Red solid (dashed) curves indicate PE → EKE conversions over the full water column (top 300 m); blue solid (dashed) curves indicate MKE → EKE conversions over the full water column (top 300 m), and yellow solid curves indicate the total EKE production. The northern sponger layer is shadowed in all panels. (For interpretation of the references to color in this figure legend, the reader is referred to the web version of this article.)

Appendix B) due to the eddy momentum flux convergence into the Core region.

A closer inspection of Fig. 8(b)–(d) reveals that the models differ in a number of ways. First, MITgcm possesses the largest fluctuations in both barotropic and baroclinic energy conversion rates as functions of latitude. For instance, the highest total EKE production rate (yellow curves in Fig. 8(b)–(d)) is approximately 2.5×10^{-5} $m^2 \cdot s^{-3}$ in MITgcm and approximately 1.5×10^{-5} $m^2 \cdot s^{-3}$ in both ROMS and HIM. Consequently, MITgcm supports the largest net EKE gain, followed by ROMS and then HIM (Table 2). Given the almost identical profiles in Fig. 8(a), the higher EKE generation in MITgcm compared to ROMS indicates greater energy dissipation as well. Second, the baroclinic EKE consumption close to the slope is more pronounced in ROMS than in MITgcm and HIM; the rate of production of PE from EKE in ROMS is more than three times higher than that in either MITgcm or HIM within the slope region (Table 2). This is likely associated with ROMS' terrain-following coordinate system, which avoids the spurious mixing and dissipation over "staircase" topography present in geopotential-coordinate models like MITgcm (Griffies et al., 2000a). Meanwhile HIM simulates lower EKE and weaker EKE production than the other models (Fig. 8(a)), so less EKE is available for conversion to PE close to the sloping topography. Third, some spikes can be seen in the profiles shown in Fig. 8(b), again a consequence of the "staircase" representation of topography in MITgcm. Fourth, the Reynolds stress work profiles derived from MITgcm and ROMS indicate three retrograde jet cores, whereas only two are evident in the HIM simulation. Various factors could contribute to a change in the number of jets (*e.g.* Vallis and Maltrud, 1993; Thompson and Young, 2007), so a suite of simulations conducted using each of these three models would likely be required to fully explain this inter-model discrepancy.

4.3. PV mixing and ageostrophic circulation

In Section 3 we showed that eddies flux PV downgradient over the continental slope, coinciding with downgradient thickness fluxes but upgradient lateral buoyancy fluxes close to the ocean bed. This suggests that the slope-trapped prograde flows might be understood via statistical mechanical arguments, specifically entropy maximization or mean enstrophy minimization, often referred to as the "Neptune effect" (Holloway, 1992; Venaille et al., 2012). We now explore whether ROMS and HIM reproduce this dynamical regime over the slope.

The blue/green curves in Fig. 5 show the profiles of background PV $\overline{q_\theta}$, offshore eddy PV fluxes F_q, and PV diffusivity κ_θ as functions of latitude from ROMS/HIM on selected isopycnal surfaces. In general, background PV is dominated by planetary vortex stretching and thus decreases with latitude over the slope and deep ocean regions. In the deep ocean the mean PV differs by a factor of ~ 1.5 between the models, but the mean PV gradients are consistently small. Over the slope, however, the PV gradients exhibit substantial inter-model differences, varying by an order of magnitude between models close to the shelf break $y \approx 170$ km. This indicates that the models' stratifications at the shelf break are sensitive to the quantitative differences in eddy behavior, *e.g.* as diagnosed from the momentum and energy budgets, in part because the continental shelf stratification is least constrained by the northern sponge layer. Fig. 5(b) shows that eddies consistently drive downgradient and upgradient PV fluxes over the slope and in the deep ocean, respectively. Near the shelf break, local maxima of eddy PV flux are visible in all models, coinciding with locations where EKE is converted into PE (Fig. 8(b)–(d)). The stronger deep-ocean upgradient eddy PV fluxes in MITgcm and ROMS are consistent with the stronger eddy momentum flux convergence in these models (Fig. 6(b)–(d)). Despite these discrepancies, a dynamical transition between slope and deep ocean is evident in all of the models.

Fig. 9 shows the mean, eddy and isopycnal overturning streamfunctions diagnosed from the ROMS and HIM shelf/slope simulations (superscripts "R" and "H" respectively correspond to ROMS and HIM). These circulations are qualitatively similar to that of the MITgcm simulation, with strong compensating mean and eddy overturning streamfunctions displaced offshore and circulations of opposite sign trapped close to the ocean bed over the slope. Close to the ocean bed, the downgradient PV flux in all models (Fig. 5(c)) is supported by a downgradient thickness flux and upgradient buoyancy flux Fig. 9(c) and (d). Thus the slope-trapped dynamical regime is a model-independent feature, though it exhibits substantial quantitative inter-model variations.

For example, while ROMS exhibits two slope-trapped mean/eddy overturning circulations, as in MITgcm, only one slope-trapped overturning cell is visible in HIM (*e.g.* compare Fig. 9, panels (a) and (b)), paralleling the reduced number of retrograde jet cores at the surface. Additionally, based on (7), the stronger (weaker) mean overturning circulation at the shelf break in ROMS (HIM) implies locally larger (smaller) divergence in eddy fluxes of retrograde momentum, consistent with the eddy momentum budget in Fig. 6. The stronger negative mean slope-trapped overturning circulation in ROMS is accompanied by a stronger positive eddy circulation, and thus greater conversion of EKE to PE close to the ocean bed, consistent with Fig. 8 and Table 2. This highlights a key difference between the MITgcm and ROMS simulations, which have very similar momentum and energy budgets (Figs. 6–8): in ROMS, EKE generated close to the surface over the slope is much more efficiently converted to PE at the ocean bed (Table 2), yielding substantially stronger slope-trapped prograde flows (Fig. 6(a)), and consequently demanding greater export of retrograde momentum to the deep ocean.

4.4. Linear stability analysis

Despite the various quantitative inter-model discrepancies, all of the model simulations show the same qualitative features, namely, lateral eddy export of momentum, surface-trapped baroclinic instabilities, and the slope-trapped upgradient buoyancy fluxes. We now ask: to what extent can these features and their inter-model variations be captured by linear stability analysis, which has been widely used to understand topography-flow interactions and been shown to have skill in predicting nonlinear eddy behaviors in prograde shelf break currents (*e.g.* Spall, 2004; Isachsen, 2011; Pennel et al., 2012; Poulin et al., 2014)?

To answer this, we perform calculations over the continental slope using the linearized quasigeostrophic (QG) equations (*e.g.* Smith, 2007 and Isachsen, 2011),

$$\begin{aligned} &q_t + J(\Psi, q) + J(\psi, Q) = 0, \quad -H < z < 0, \\ &b_t + J(\Psi, b) + J(\psi, B) = 0, \quad z = 0, \\ &b_t + J(\Psi, b) + J(\psi, B) + J(\psi, S)B_z = 0, \quad z = -H, \end{aligned} \tag{12}$$

where $q = \nabla^2\psi + \Gamma\psi$ is the QG potential vorticity (PV) perturbation, $\Gamma = \frac{\partial}{\partial z}\left(\frac{f_0^2}{N^2}\frac{\partial}{\partial z}\right)$ is conventionally defined as the vortex stretching operator (Smith, 2007; Tulloch et al., 2011), ψ denotes the QG eddy streamfunction, $b = f_0\frac{\partial\psi}{\partial z}$ corresponds to buoyancy perturbation, and S is the sea floor height. The mean geostrophic streamfunction, background QG PV, and mean buoyancy are denoted as Ψ, Q, and B, respectively. Below we solve (12) for the unknown perturbations ψ and q, deriving Ψ, Q and B from the mean states of our nonlinear simulations.

Substituting the wave solution of the form

$$\psi = \Phi(z)e^{i(kx+ly-\omega t)} \tag{13}$$

into (12) yields

$$\begin{aligned} &\omega(\Gamma - k^2 - l^2)\Phi = [kQ_y + k\overline{u}(\Gamma - k^2 - l^2)]\Phi, \quad -H < z < 0, \\ &(-\omega + k\overline{u})\frac{\partial\Phi}{\partial z} - k\frac{\partial\overline{u}}{\partial z}\Phi = 0, \quad z = 0, \\ &(-\omega + k\overline{u})\frac{\partial\Phi}{\partial z} - k\left(\frac{\partial\overline{u}}{\partial z} - \frac{N^2}{f_0}S_y\right)\Phi = 0, \quad z = -H, \end{aligned} \tag{14}$$

where the ageostrophic meridional velocity has been excluded (*e.g.* Pedlosky, 1987 and Vallis, 2006). Here Q_y is the background QG PV gradient and S_y is the horizontal gradient of the sea floor height with

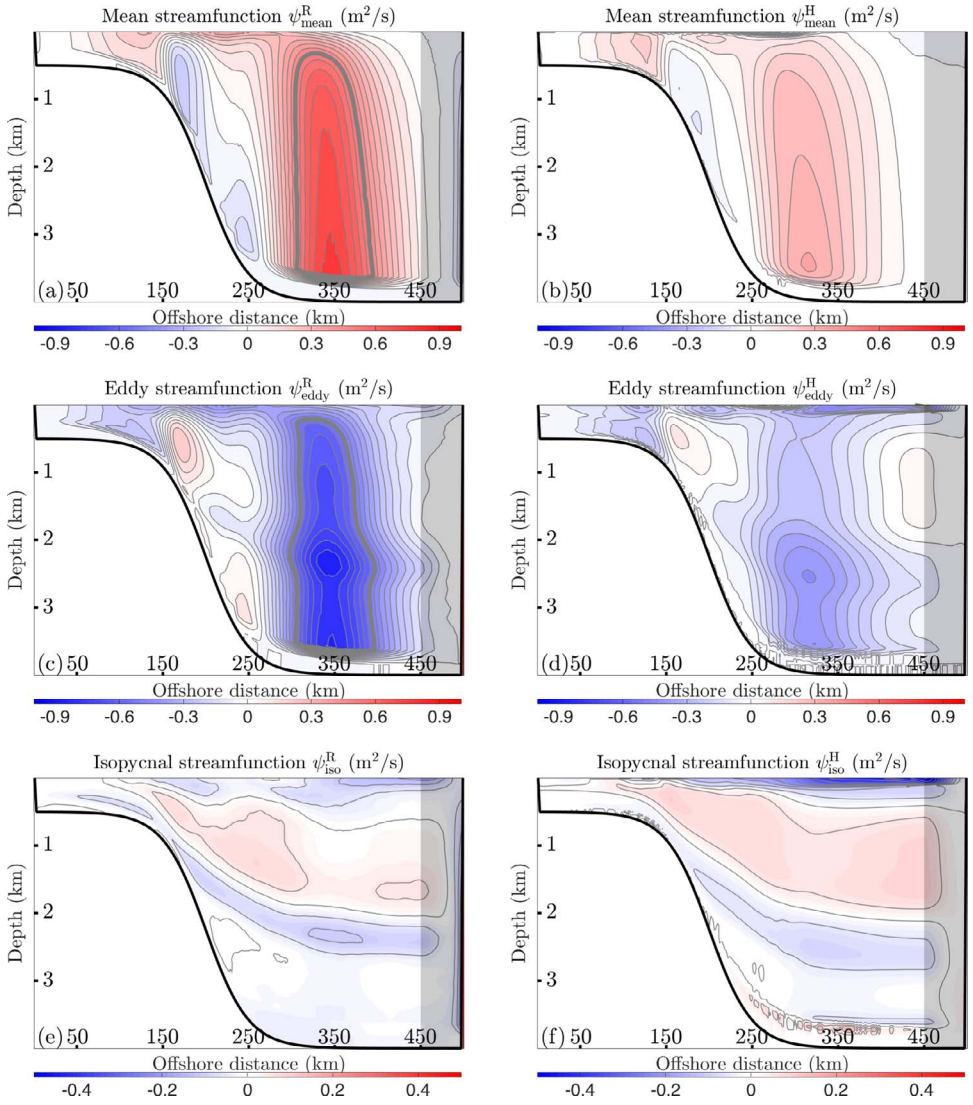

Fig. 9. Mean overturning streamfunctions diagnosed from (a) ROMS and (b) HIM shelf/slope simulations. Positive (negative) contours denote clockwise (counterclockwise) circulation. The 0.5 m^2/s streamline is indicated by a bold gray contour. Eddy overturning streamfunctions diagnosed from (c) ROMS and (d) HIM shelf/slope simulations. The – 0.5 m^2/s streamline is indicated by a bold gray contour. Isopycnal overturning streamfunctions diagnosed from (e) ROMS and (f) HIM shelf/slope simulations. The northern sponge layer is shadowed in all panels.

respect to latitude. Eq. (14) comprises an eigenvalue problem in terms of the complex frequency ω, with eigenfunctions that correspond to the vertical structure Φ. We solve this eigenvalue problem numerically via vertical discretization of Φ as described by Smith (2007). Following Tulloch et al. (2011), any unstable modal solution of (14) with wavenumber larger than five times of the inverse deformation radius is abandoned as our model runs barely resolve them in the presence of steep slopes.

Several caveats should be stressed prior to discussing the linear solutions. First, (12) holds only if the horizontal variations of mean stratification B_z are negligible (*e.g.* Pedlosky, 1987 and Vallis, 2006), a condition that is violated by our primitive equation simulations. Nevertheless, such a procedure proved successful in qualitatively understanding eddy field over continental slopes around the Lofoten Basin, across which stratification changes sharply (Isachsen, 2015). Second, previous QG analysis reveals that ignoring the horizontal shear of velocity may lead to qualitative errors in linear solutions (Killworth, 1980). Over steep slopes, mean relative vorticity may even dominate the background QG PV and hence impact the growth rates and length scales of baroclinic unstable waves (Isachsen, 2015). We therefore have retained the relative vorticity component when defining Q.[3] Finally, analogous to (Isachsen, 2011; 2015), the slope here only enters the QG equations via bottom PV sheets in the bottom boundary condition of (12). In contrast, our simulations exhibit isopycnal outcropping along the slope, an effect that cannot be captured in a QG model.

Fig. 10(a) shows the normalized vertical structure Φ of the fastest growing modes at y = 200 km latitude, where the bottom slope is steepest. The fastest-growing modes are all purely meridional "noodle" modes, *i.e.* having meridional wave number l=0, (Chen and Kamenkovich, 2013), in both the shelf/slope and flat-bottom simulations. Using the mean state from the shelf/slope runs, all models produce unstable linear modes that are strongly surface-intensified, in qualitative agreement with the surface-confined baroclinic energy production shown in Fig. 3. In contrast, in the flat-bottom cases the unstable modal structures are of comparable magnitude throughout the water column, consistent with the baroclinic energy production at depth in Fig. 7(b) (see also Appendix B). Thus while there are quantitative inter-model discrepancies in the vertical structures of the solutions, both in the shelf/slope and flat-bottom simulations, it seems that the surface intensification of baroclinic energy is explained by linear theory, and specifically by suppression of baroclinic instability by the

[3] Inclusion of mean relative vorticity also makes linear calculations two-dimensional by

(*footnote continued*)
encompassing barotropic modes, which we have chosen to leave out by imposing (13) because it is the baroclinic instability that serves to generate eddies in our simulations.

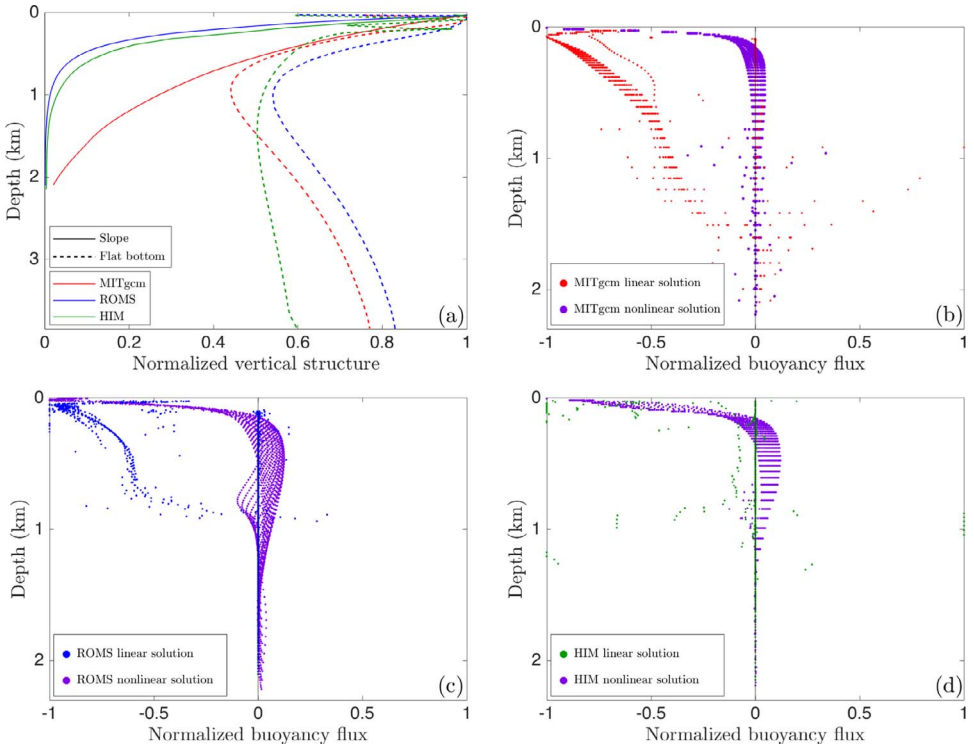

Fig. 10. (a) Normalized vertical structures of the most unstable linear modes derived from shelf/slope (solid curves) and flat-bottom (dashed curves) simulations using MITgcm, ROMS and HIM. (b)–(d) Normalized eddy buoyancy flux calculated from the fully nonlinear model solutions (purple dots) and linear stability analysis (red, blue, and green dots) over the shoreward half of continental slope in the three models. (For interpretation of the references to color in this figure legend, the reader is referred to the web version of this article.)

topographic PV gradient.

In our nonlinear simulations, the lower part of the water column over the slope exhibits laterally upgradient buoyancy fluxes and EKE consumption. Fig. 10(b)–(d) compares the buoyancy fluxes predicted by linear theory against those diagnosed from our nonlinear simulations. In the linear QG theory, the lateral time-/zonal-mean buoyancy flux can be written as

$$F_b = \frac{1}{2}k_c f_0 \left(\Phi_r \frac{\partial \Phi_i}{\partial z} - \Phi_i \frac{\Phi_r}{\partial z}\right) e^{2\omega_i t}, \tag{15}$$

where k_c is the wavenumber of most unstable wave, Φ_r (Φ_i) denotes the real (imaginary) part of its structural coefficient $\Phi(z)$, and ω_i is the growth rate. As the wave growth is positive definite, we focus on the time-independent factor of F_b only. We focus on linear solutions and nonlinear fluxes derived from latitudes between $y = 150$ km and $y = 200$ km, where upgradient buoyancy fluxes appear consistently in the nonlinear model simulations.

The nonlinear solutions consistently produce relatively large downgradient (shoreward) buoyancy fluxes in the upper few hundred meters of the water column, overlying upgradient (offshore) buoyancy fluxes in the deeper portions of the water column. While the linear solutions also predict strong downgradient buoyancy fluxes close to the surface, in the subsurface these fluxes remain downgradient and gradually decrease in magnitude with depth. While the linear buoyancy fluxes are very slightly upgradient in a few locations, overall the linear prediction is qualitatively different from the nonlinear realizations. This disagreement reinforces our conclusion that the upgradient buoyancy fluxes and the associated consumption of EKE close to the slope are sustained via non-local sources of EKE. Linear stability analysis is built on local mean flow field alone, and appears to be incapable of reproducing this phenomenon. Additionally, the linear solutions predict a lateral eddy momentum flux $F_m = \frac{1}{2}\phi^2(z)k_c l_c$ (Warneford and Dellar, 2017) that is identically zero for any "noodle" mode (*i.e.* $l_c = 0$), where l_c denotes the meridional wave number of the most unstable modal solution. The linear predictions therefore also fail to capture the strong offshore flux of retrograde momentum and associated Reynods stress convergence of energy.

5. Summary and conclusion

Eddies over continental slopes play a key role in shaping water mass formations and the ocean general circulation (Spall, 2004; Brink, 2016b; Stewart and Thompson, 2015a). Nonlinear eddy behaviors resulting from instabilities of prograde baroclinic currents have been shown to be well explained by the linear phase of baroclinic growth, in contrast to retrograde baroclinic currents (Spall, 2004; Isachsen, 2011; Pennel et al., 2012). In this article, we have studied baroclinic turbulence over an idealized continental slope under retrograde winds using three numerical ocean models that span the range of commonly used vertical coordinate systems. Results that are consistently reproduced between these models are inferred to be insensitive to the discrete representation of flow over topography, and therefore most physically robust. Quantitative discrepancies among models are related to multiple differences in the numerical algorithms listed in Section 2. The sources of numerical error (*e.g.* in the momentum budgets) are also model-dependent. We therefore refrain from offering comment on which model performs best in this application.

Our reference simulations share several key features that distinguish shelf/slope baroclinic turbulence from the case of a flat ocean bed. Momentum imparted by surface wind stress is exported laterally by eddies in the top few hundred meters, shifting the thermal shear current offshore. This offshore retrograde momentum flux, combined with the formation of multiple retrograde jet cores separated approximately by the topographic Rhines scale (Rhines, 1975; Vallis and Maltrud, 1993) leads to a series of barotropic energy conversions of alternating signs. This eddy momentum transfer is intrinsically nonlinear in nature and cannot be reproduced using QG linear stability theory. In the open ocean, eddy momentum flux is dominantly downward and balanced by bottom drag. When the continental slope is replaced by a flat ocean bed, momentum is instead transfered directly downward and locally extracted via bottom drag.

In our model runs, the eddies are principally generated by baroclinic instabilities confined within the uppermost few hundred meters of the water column, consistent with the local linear stability analysis and prior studies based on analytical QG models (*e.g.* Chen and

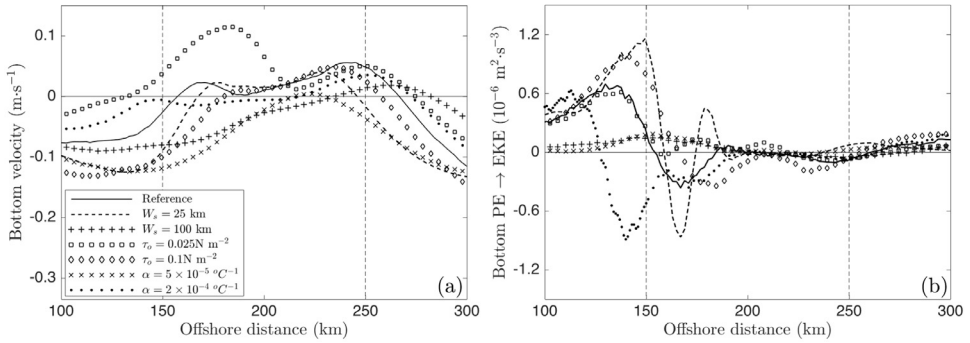

Fig. 11. (a) Time-/zonal-mean bottom velocity profiles produced by sensitivity simulations as functions of offshore distance. (b) Time-/zonal-mean conversion rates of PE into EKE integrated over the bottom 300 m as functions of offshore distance. Each simulation is denoted by a distinct line type with a key physical parameter altered indicated by the inner panel of (a) contrasted to the reference run. The reference run is indicated by solid lines.

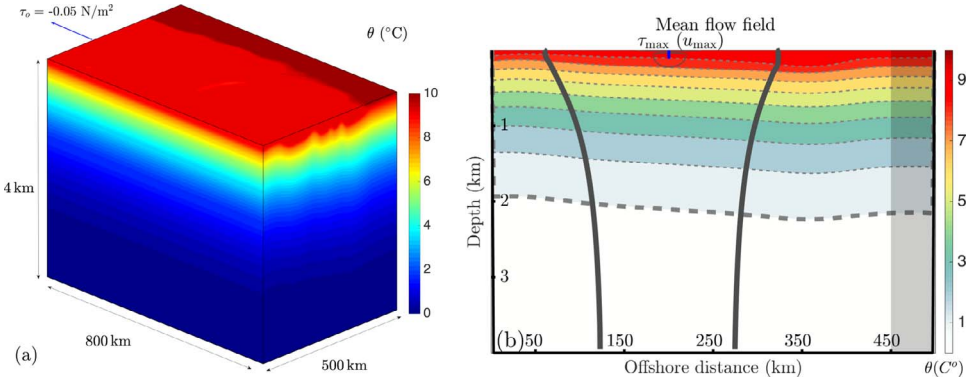

Fig. 12. Reproduction of Fig. 1 for flat-bottomed run. All physical parameters are identical to that of the reference shelf/slope run except that the continental slope is replaced with a uniform planetary vorticity gradient across the channel.

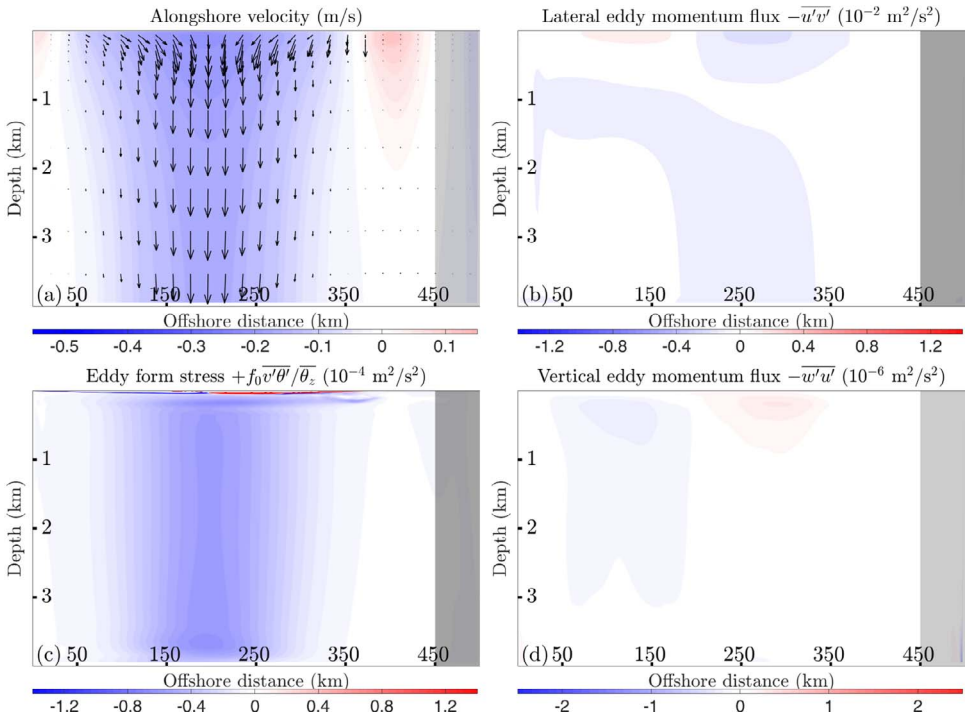

Fig. 13. Reproduction of Fig. 2 for flat-bottomed run.

Kamenkovich, 2013). Away from the slope, baroclinic instabilities penetrate to depth as topographic suppression is mitigated. This EKE generation serves as a non-local driver of PE production close to the sloping ocean bed, acting to tilt isopycnals and accelerate prograde near-bottom flows. This consumption of EKE is associated with down-gradient eddy PV and thickness fluxes, but upgradient lateral buoyancy fluxes. The near-slope dynamics are therefore qualitatively consistent with the "Neptune effect" (Holloway, 1992), in which eddies drive prograde flows as the system tends toward a state of maximum entropy, or minimum mean potential enstrophy (Venaille et al., 2012). Additional spin-down simulations will be required to further validate this effect. The non-local energetics associated with this dynamical regime place it beyond the scope of linear theory.

The angle of bottom topography in our reference simulation is approximately 2^o and thus falls within the average range of steepness of realistic continental slopes (*e.g.* Cacchione et al. 2002). We have also

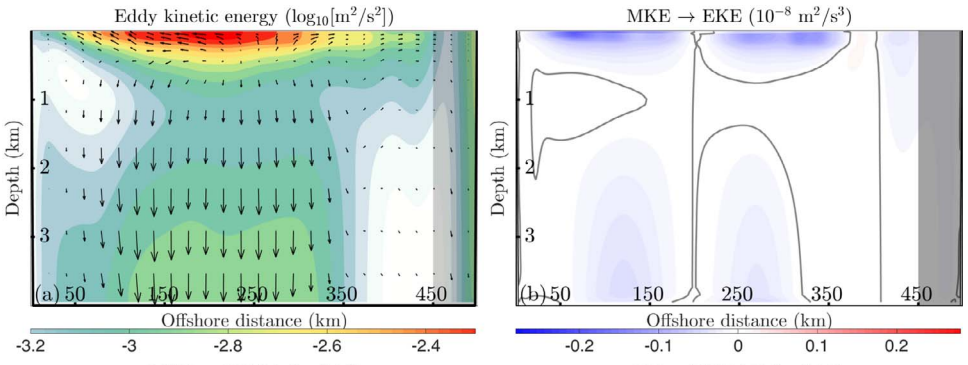

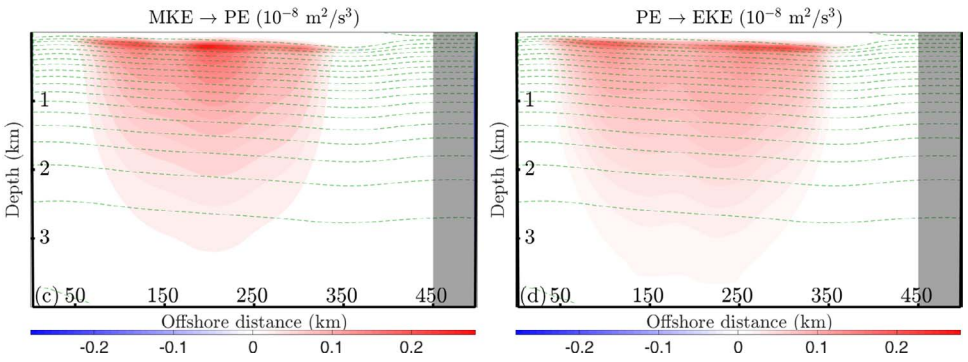

Fig. 14. Reproduction of Fig. 3 for flat-bottomed run. Color ranges are adjusted for improved visualization.

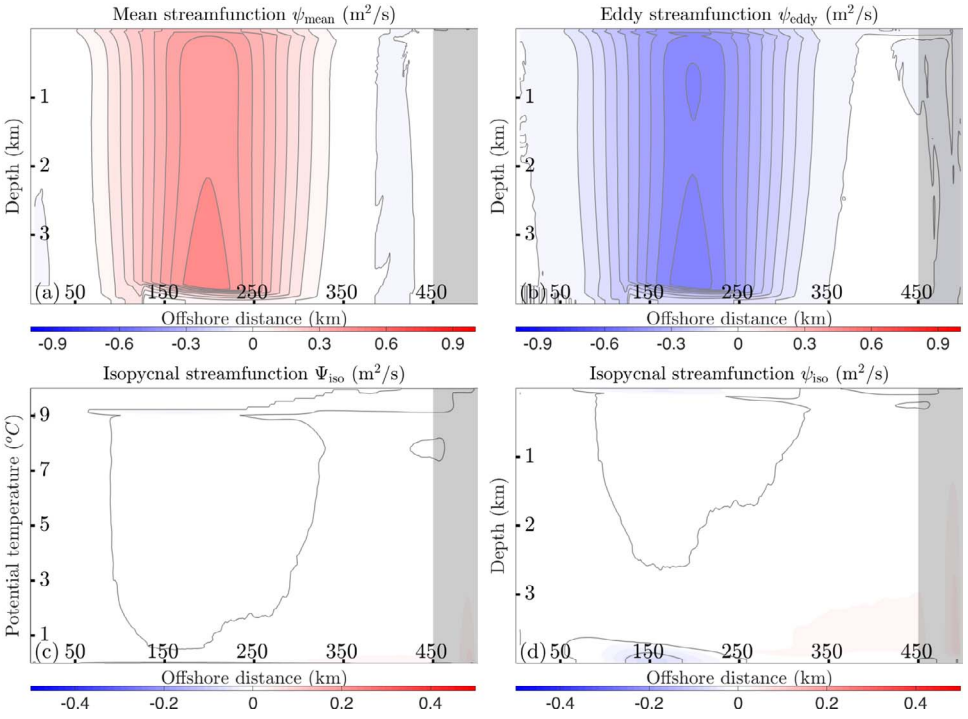

Fig. 15. Reproduction of Fig. 4 for flat-bottomed run.

performed a series of sensitivity runs based on MITgcm[4] to further verify the applicability of our results by varying key physical parameters, namely the slope width (to 50 km or 200 km), the wind stress maximum (to 0.025 N m^{-2} or 0.1 N m^{-2}), and the thermal expansion coefficient (to 5×10^{-5} $^oC^{-1}$ or 2×10^{-4} $^oC^{-1}$). All sensitivity runs reproduce the key turbulent properties discussed in Section 3:

- Momentum injected by wind is exported laterally by eddies over the top few hundred meters (*c.f.* Sections 3.2 and 4.1).
- Baroclinic instabilities are trapped within the top few hundred meters (*c.f.* Sections 3.3 and 4.2).
- The conversion of EKE into PE dominates the slope-trapped flows, corresponding to upgradient eddy buoyancy fluxes (*c.f.* Sections 3.3, 4.2, and 4.4).

Here we briefly explore the robustness of the sloping-bottom-trapped flows under alternative physical conditions. Fig. 11(a) shows

[4] Since almost no difference is yielded by replacing the KPP in the reference run with a large diffusivity (100 m^2/s) for parameterizing convective instabilities in MITgcm, all sensitivity runs follow this setting for computational efficiency.

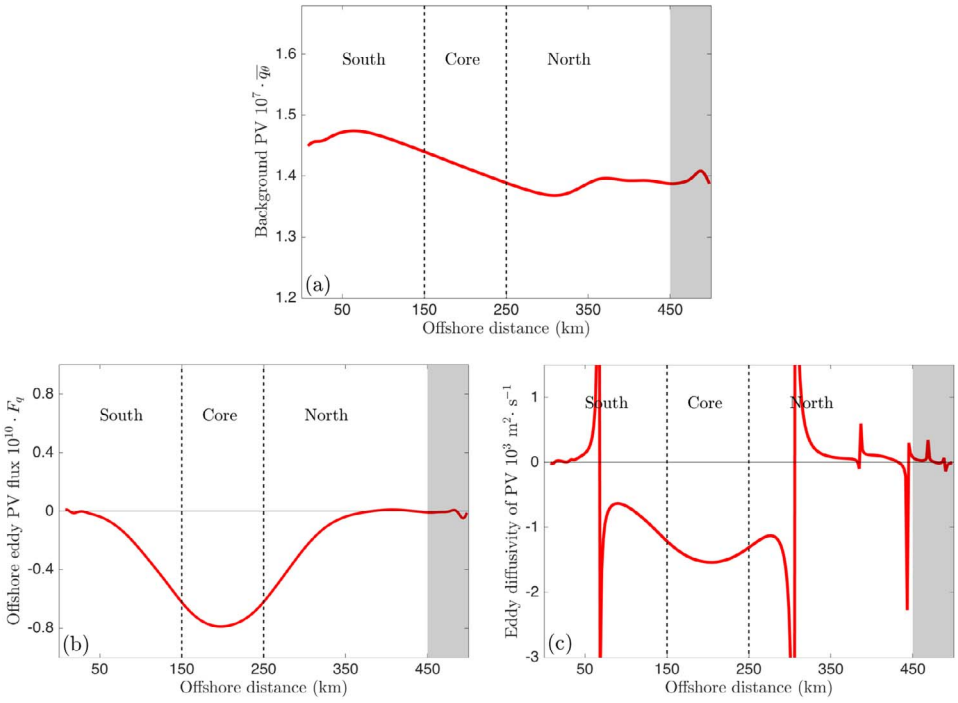

Fig. 16. Reproduction of Fig. 5 for MITgcm flat-bottomed run. Axis ranges are adjusted for improved visualization.

the bottom along-slope velocity profiles as functions of offshore distance after time-/zonal-mean. All sensitivity simulations produce prograde flows, though with deviating magnitudes and locations. The weakest prograde jet is supported by the least stratified flow (with halved thermal expansion coefficient contrasted to the reference run). Accordingly, Fig. 11(b), which shows the time-/zonal-averages of conversion rate of PE into EKE integrated over the bottom 300 m as functions of latitude, suggests that all prograde flows are accompanied by generation of PE from EKE, though this association is less obvious for weakly stratified flows. We also note that previous model studies, *e.g.* of the California Current system (Fig. 4 of Colas et al. 2013) and the Antarctic Slope Front (Fig. 7(a) of Stewart and Thompson 2016), exhibit EKE consumption close to the continental slope, lending additional support to our conclusions and their applicability to the ocean (Figs 12–16).

Though our findings are qualitatively consistent across different models and sensitivity simulations in parameter ranges relevant to the oceans, our study carries a number of caveats associated with our idealized model configuration. For instance, the simulations do not include zonal variations in bottom topography, which can alter the zonal momentum budget (11) via bottom form drag (*e.g.* Molemaker et al., 2015). Additionally, curvature in the continental slope modifies the growth of baroclinic instabilities (Solodoch et al., 2016) and favors breaking of topographic Rossby waves (Stewart et al., 2014; 2011). Buoyancy forcing can also effectively shape the flow field over continental slopes and modulate the PV field. We have neglected tides, which often play a non-negligible role in forming shelf break fronts (*e.g.* Brink 2012; 2013). Finally, we have not incorporated temporal variations in surface wind stress, which can impact eddy variabilities over continental slopes (Zhai and Greatbatch, 2007; Renault et al., 2016).

Further work is required to develop a predictive theory relating the bottom slope and forcing to the resulting mean flow and cross-slope eddy transfer. Expanding our sensitivity simulations and developing such a theory is the subject of ongoing work. However, our findings do suggest that any parameterization for eddy transfer across continental slopes must include an explicit treatment of the eddy momentum fluxes, which make a leading-order contribution to the mean circulation in our model runs. The downgradient mixing of PV over the slope suggests that a PV-based, rather than buoyancy-based, approach to parameterizing eddies over steep slopes may be necessary.

Acknowledgments

The authors are thankful to Kaushik Srinivasan for his help with ROMS. This work used the Extreme Science and Engineering Discovery Environment (XSEDE, Towns et al., 2014), which is supported by National Science Foundation grant number ACI-1548562. YW and ALS are supported by National Science Foundation, grant number OCE-1538702. The authors thank G. E. Manucharyan and an anonymous reviewer for comments that improved this article.

Appendix A. Depth-integrated momentum budget for HIM

Here we briefly describe the calculation of depth-integrated momentum budget for HIM. A total of four individual terms are shown in Fig. 6(d).

The wind stress input term is simply (2) divided by ρ_0 and consistent across models.

The depth-averaged advection and Coriolis acceleration terms (located at velocity-points of numerical grid boxes) in conjunction with the layer thicknesses (located at mass-points of numerical grid boxes) are readily output from the HIM code. The only modification needed for obtaining the depth-integrated terms is to linearly interpolate the water column height from mass- onto velocity-points for computational accuracy.

The calculation of bottom drag follows exactly the algorithm provided by HIM code, which is based on a quadratic drag law and computes the friction velocity assigned to the bottom 10 m (a default value in HIM) from the solutions of velocity field and layer thicknesses.

Appendix B. Diagnostics from MITgcm flat-bottomed run

Here we reproduce the same plots as in Section 3 for the flat-bottomed run of MITgcm as a reference. For better illustration the value ranges of some diagnostics are modified compared to those in Section 3 and noted in the figure captions.

References

Abernathey, R., Ferreira, D., Klocker, A., 2013. Diagnostics of isopycnal mixing in a circumpolar channel. Ocean Modell. 72, 1–16. http://dx.doi.org/10.1016/j.ocemod.2013.07.004.

Arakawa, A., Hsu, Y.G., 1990. Energy conserving and potential-enstrophy dissipating schemes for the shallow water equations. Mon. Weather Rev. 118 (10), 1960–1969. http://dx.doi.org/10.1175/1520-0493(1990)118<1960:ECAPED>2.0.CO;2.

Blumsack, S.L., Gierasch, P.J., 1972. Mars: the effects of topography on baroclinic instability. J. Atmos. Sci. 29 (6), 1081–1089. http://dx.doi.org/10.1175/1520-0469(1972)029<1081:MTEOTO>2.0.CO;2.

Boccaletti, G., Ferrari, R., Fox-Kemper, B., 2007. Mixed layer instabilities and restratification. J. Phys. Oceanogr. 37, 2228–2250.

Bretherton, F.P., Haidvogel, D., 1976. Two-dimesional turbulence over topography. J. Fluid Mech. 78, 129–154.

Brink, K.H., 2012. Baroclinic instability of an idealized tidal mixing front. J. Mar. Res. 70 (4), 661–688.

Brink, K.H., 2013. Instability of a tidal mixing front in the presence of realistic tides and mixing. J. Mar. Res. 71 (3), 227–251.

Brink, K.H., 2016a. Continental shelf baroclinic instability. part I: relaxation from upwelling or downwelling. J. Phys. Oceanogr. 46, 551–568. http://dx.doi.org/10.1175/JPO-D-15-0047.1.

Brink, K.H., 2016b. Cross-shelf exchange. Annu. Rev. Fluid Mech. 8, 59–78.

Brink, K.H., Seo, H., 2016. Continental shelf baroclinic instability. part II: oscillating wind forcing. J. Phys. Oceanogr. 46, 569–582. http://dx.doi.org/10.1175/JPO-D-15-0048.1.

Cacchione, D.A., Pratson, L.F., Ogston, A.S., 2002. The shaping of continental slopes by internal tides. Science 296 (5568), 724–727. http://dx.doi.org/10.1126/science.1069803.

Capet, X., McWilliams, J.C., Molemaker, M.J., Shchepetkin, A.F., 2008a. Mesoscale to submesoscale transition in the California current system. Part I: flow structure, eddy flux, and observational tests. J. Phys. Oceanogr. 38, 29–43.

Capet, X., McWilliams, J.C., Molemaker, M.J., Shchepetkin, A.F., 2008b. Mesoscale to submesoscale transition in the California current system. Part II: frontal processes. J. Phys. Oceanogr. 38, 44–64.

Capet, X., McWilliams, J.C., Molemaker, M.J., Shchepetkin, A.F., 2008c. Mesoscale to submesoscale transition in the California current system. Part III: energy balance and flux. J. Phys. Oceanogr. 38, 2256–2269.

Chang, E.M., Orlanski, I., 1993. On the dynamics of a storm track. J. Atmos. Sci. 50, 999–1015. http://dx.doi.org/10.1175/1520-0469(1993)050<0999:OTDOAS>2.0.CO;2.

Chapman, C.C., Hogg, A.C., Kiss, A.E., Rintoul, S.R., 2015. The dynamics of Southern ocean storm tracks. J. Phys. Oceanogr. 45, 884–903. http://dx.doi.org/10.1175/JPO-D-14-0075.1.

Chassignet, E.P., Arango, H., Dietrich, D., Ezer, T., Ghil, M., Haidvogel, D.B., Ma, C.C., Mehra, A., Paiva, A.M., Sirkes, Z., 2000. Damee-nab: the base experiments. Dynam. Atmos. Ocean. 32, 155–183.

Chassignet, E.P., Hurlburt, H.E., Smedstad, O.M., Halliwell, G.R., Hogan, P.J., Wallcraft, A.J., Bleck, R., 2006. Ocean prediction with the Hhybrid coordinate ocean model (HYCOM). In: Chassignet, E.P., Verron, J. (Eds.), Ocean Weather Forecasting: An Integrated View of Oceanography. Springer, pp. 413–436.

Chassignet, E.P., Smith, L.T., Bleck, R., Bryan, F.O., 1996. A model comparison: numerical simulations of the North and Equatorial Atlantic oceanic circulation in depth and isopycnic coordinates. J. Phys. Oceanogr. 26, 1849–1867.

Chen, C., Kamenkovich, I., 2013. Effects of topography on baroclinic instability. J. Phys. Oceanogr. 43 (4), 790–804. http://dx.doi.org/10.1175/JPO-D-12-0145.1.

Chen, R., Flierl, G.R., Wunsch, C., 2014. A description of local and nonlocal eddy-mean flow interaction in a global eddy-permitting state estimate. J. Phys. Oceanogr. 44 (9), 2336–2352. http://dx.doi.org/10.1175/JPO-D-14-0009.1.

Colas, F., Capet, X., McWilliams, J.C., Li, Z., 2013. Mesoscale eddy buoyancy flux and eddy-induced circulation in Eastern Boundary Currents. J. Phys. Oceanogr. 43 (6), 1073–1095. http://dx.doi.org/10.1175/JPO-D-11-0241.1.

Dinniman, M.S., Klinck, J.M., Jr., W.O.S., 2011. A model study of circumpolar deep water on the West Antarctic Peninsula and Ross Sea continental shelves. Deep Sea Res. Pt. II 58 (13–16), 1508–1523. http://dx.doi.org/10.1016/j.dsr2.2010.11.013.

Dong, C., McWilliams, J.C., Liu, Y., Chen, D., 2014. Global heat and salt transports by eddy movement. Nat. Comm. 5, 3294.

Eady, E.T., 1949. Long waves and cyclone waves. Tellus 1, 33–52.

Ezer, T., 2016. Revisiting the problem of the Gulf Stream separation: on the representation of topography in ocean models with different types of vertical grids. Ocean Modell. 104, 15–27. http://dx.doi.org/10.1016/j.ocemod.2016.05.008.

Ezer, T., Mellor, G.L., 2004. A generalized coordinate ocean model and a comparison of the bottom boundary layer dynamics in terrain-following and in z-level grids. Ocean Modell. 6 (3–4), 379–403. http://dx.doi.org/10.1016/S1463-5003(03)00026-X.

Fox-Kemper, B., Ferrari, R., Hallberg, R., 2008. Parameterization of mixed layer eddies. part I: theory and diagnosis. J. Phys. Oceanogr. 38 (6), 1145–1165. http://dx.doi.org/10.1175/2007JPO3792.1.

Gent, P.R., 2011. The Gent-McWilliams parameterization: 20/20 hindsight. Ocean Modell. 39 (1–2), 2–9. http://dx.doi.org/10.1016/j.ocemod.2010.08.002.

Griffies, S.M., Böning, C., Bryan, F.O., Chassignet, E.P., Gerdes, R., Hasumi, H., Hirst, A., Treguier, A., Webb, D., 2000a. Developments in ocean climate modelling. Ocean Modell. 2, 123–192.

Griffies, S.M., Pacanowski, R.C., Hallaberg, R.W., 2000b. Spurious diapycnal mixing associated with advection in a z-coordinate ocean model. J. Phys. Oceanogr. 128, 538–564.

Hallberg, R., 2013. Using a resolution function to regulate parameterizations of oceanic mesoscale eddy effects. Ocean Modell. 72, 92–103. http://dx.doi.org/10.1016/j.ocemod.2013.08.007.

Hallberg, R., Rhines, P., 1996. Buoyancy-driven circulation in an ocean basin with isopycnals intersecting the sloping boundary. J. PhyS. Oceanogr 26 (6), 913–940. http://dx.doi.org/10.1175/1520-0485(1996)026<0913:BDCIAO>2.0.CO;2.

Hattermann, T., Smedsrud, L.H., Nst, O.A., Lilly, J.M., Galton-Fenzi, B.K., 2014. Eddy-resolving simulations of the Fimbul Ice Shelf cavity circulation: basal melting and exchange with open ocean. Ocean Modell. 82, 28–44. http://dx.doi.org/10.1016/j.ocemod.2014.07.004.

Hetland, R.D., 2017. Suppression of baroclinic instabilities in buoyancy-driven flow over sloping bathymetry. J. Phys. Oceanogr. 47 (1), 49–68. http://dx.doi.org/10.1175/JPO-D-15-0240.1.

Hill, C., Ferreira, D., Campin, J., Marshall, J., Abernathey, R., Barrier, N., 2012. Controlling spurious diapycnal mixing in eddy-resolving height-coordinate ocean models - insights from virtual deliberate tracer release experiments. Ocean Modell. 45, 14–26. http://dx.doi.org/10.1016/j.ocemod.2011.12.001.

Holloway, G., 1978. A spectral theory of nonlinear barotropic motion above irregular topography. J. Phys. Oceanogr. 8 (3), 414–427. http://dx.doi.org/10.1175/1520-0485(1978)008<0414:ASTONB>2.0.CO;2.

Holloway, G., 1986. Eddies, waves, circulation, and mixing: statistical geofluid mechanics. Ann. Rev. Fluid. Mech. 18, 91–147.

Holloway, G., 1992. Representing topographic stress for large-scale ocean models. J. Phys. Oceanogr. 22 (9), 1033–1046. http://dx.doi.org/10.1175/1520-0485(1992)022<1033:RTSFLS>2.0.CO;2.

Holloway, G., 1993. Overview of statistical mechanics, with practical application for ocean modeling. Statistical Methods in Physical Oceanography: Proceedings, 'Aha Huliko'a Hawaiian Winter Workshop, University of Hawaii at Manoa, January 12–15, 1993. School of Ocean and Earth Science and Technology, pp. 491.

Holloway, G., 1996. Neptune Effect: Statistical Mechanical Forcing of Ocean Circulation. Birkhäuser Boston, Boston, MA, pp. 207–219. doi:10.1007/978-1-4612-2430-3_8.

Isachsen, P.E., 2011. Baroclinic instability and eddy tracer transport across sloping bottom topography: how well does a modified Eady model do in primitive equation simulations? Ocean Modell. 39 (1–2), 183–199. http://dx.doi.org/10.1016/j.ocemod.2010.09.007.

Isachsen, P.E., 2015. Baroclinic instability and the mesoscale eddy field around the Lofoten basin. J. Geophys. Res. 120 (4), 2884–2903. http://dx.doi.org/10.1002/2014JC010448.

Jungclaus, J.H., Mellor, G.L., 2000. A three-dimensional model study of the Mediterranean outflow. J. Marine Syst. 24 (1–2), 41–66. http://dx.doi.org/10.1016/S0924-7963(99)00078-0.

Killworth, P., 1980. Barotropic and baroclinic instability in rotating stratified fluids. Dyn. Atmos. Oceans 4, 143–184.

LaCasce, J.H., 1998. A geostrophic vortex over a slope. J. Phys. Oceanogr. 28 (12), 2362–2381. http://dx.doi.org/10.1175/1520-0485(1998)028<2362:AGVOAS>2.0.CO;2.

LaCasce, J.H., Brink, K.H., 2000. Geostrophic turbulence over a slope. J. Phys. Oceanogr. 30 (6), 1305–1324. http://dx.doi.org/10.1175/1520-0485(2000)030<1305:GTOAS>2.0.CO;2.

Large, W.G., McWilliams, J.C., Doney, S.C., 1994. Oceanic vertical mixing: a review and a model with a nonlocal boundary layer parameterization. Rev. Geophys. 32, 363–403.

Legg, S., Hallberg, R.W., Girton, J.B., 2006. Comparison of entrainment in overflows simulated by z-coordinate, isopycnal and non-hydrostatic models. Ocean Modell. 11 (1–2), 69–97. http://dx.doi.org/10.1016/j.ocemod.2004.11.006.

Maltrud, M.E., McClean, J.L., 2005. An eddy resolving global 1/10° ocean simulation. Ocean Modell. 8, 31–54.

Maltrud, M.E., Vallis, G.K., 1991. Energy spectra and coherent structures in forced two-dimensional and beta-plane turbulence. J. Fluid Mech. 228, 321–342.

Maltrud, M.E., Vallis, G.K., 1992. Generation of mean flow and jets on a beta plane and over topography. J. Phys. Oceanogr. 23, 1346–1362.

Marshall, J., Adcroft, A., Hill, C., Perelman, L., Heisey, C., 1997. A finite-volume, incompressible Navier Stokes model for studies of the ocean on parallel computers. J. Geophys. Res. 102 (C3), 5753–5766. http://dx.doi.org/10.1029/96JC02775.

Marshall, J., Radko, T., 2003. Residual-mean solutions for the Antarctic Circumpolar Current and its associated overturning circulation. J. Phys. Oceanogr. 33 (11), 2341–2354. http://dx.doi.org/10.1175/1520-0485(2003)033<2341:RSFTAC>2.0.CO;2.

Marshalll, D.P., Maddison, J.R., Berloff, P.S., 2012. A framework for parameterizing eddy potential vorticity fluxes. J. Phys. Oceanogr. 42, 539–557. http://dx.doi.org/10.1175/JPO-D-11-048.1.

Mechoso, C.R., 1980. Baroclinic instability of flows along sloping boundaries. J. Atmos. Sci. 37 (6), 1393–1399.

Molemaker, M.J., McWilliams, J.C., Dewar, W.K., 2015. Submesoscale instability and generation of mesoscale anticyclones near a separation of the California Undercurrent. J. Phys. Oceanogr. 45 (3), 613–629.

Morrow, R., Church, J., Coleman, R., Chelton, D., White, N., 1992. Eddy momentum flux and its contribution to the Southern Ocean momentum balance. Nature 357,

482–484.
Nencioli, F., Petrenko, A.A., Doglioli, A.M., 2016. Diagnosing cross-shelf transport along an ocean front: an observational case study in the Gulf of Lion. J. Geophys. Res. 121 (10), 7218–7243. http://dx.doi.org/10.1002/2016JC011908.
Nøst, O.A., Biuw, M., Tverberg, V., Lydersen, C., Hattermann, T., Zhou, Q., Smedsrud, L.H., Kovacs, K.M., 2011. Eddy overturning of the Antarctic Slope Front controls glacial melting in the Eastern Weddell sea. J. Geophys. Res. 116 (C11). http://dx.doi.org/10.1029/2011JC006965.
Pedlosky, J., 1987. Geophysical Fluid Dynamics, 2nd ed.,. Springer.
Pennel, R., Orlanski, I., Béranger, K., 2012. Shelf impact on buoyant coastal current instabilities. J. Phys. Oceanogr. 42, 39–61. http://dx.doi.org/10.1175/JPO-D-11-016.1.
Pickart, R.S., Spall, M.A., 2007. Impact of Labrador sea convection on the North Atlantic meridional overturning circulation. J. Phys. Oceanogr. 37 (9), 2207–2227. http://dx.doi.org/10.1175/JPO3178.1.
Plumb, R.A., Ferrari, R., 2005. Transformed Eulerian-Mean theory. part I: nonquasigeostrophic theory for eddies on a zonal-mean flow. J. Phys. Oceanogr. 35 (2), 165–174. http://dx.doi.org/10.1175/JPO-2669.1.
Poulin, F.J., Stegner, A.A., Hernández-Arencibia, M.M., Marrero-Díaz, A.A., Sangrà, P., 2014. Steep shelf stabilization of the coastal Bransfield current: linear stability analysis. J. Phys. Oceanogr. 44, 714–732. http://dx.doi.org/10.1175/JPO-D-13-0158.1.
Prather, M.J., 1986. Numerical advection by conservation of second-order moments. J. Geophys. Res. 91 (D6), 6671–6681. http://dx.doi.org/10.1029/JD091iD06p06671.
Renault, L., Molemaker, M.J., McWilliams, J.C., Shchepetkin, A.F., Lemarié, F., Chelton, D., Illig, S., Hall, A., 2016. Modulation of wind work by oceanic current interaction with the atmosphere. J. Phys. Oceanogr. 46 (6), 1685–1704. http://dx.doi.org/10.1175/JPO-D-15-0232.1.
Rhines, P.B., 1975. Waves and turbulence on a beta-plane. J. Fluid Mech. 69. 471–443
Roberts, M.J., Wood, R.A., Marsh, R., New, A.L., 1996. An intercomparison of a Bryan-Cox-type ocean model and an isopycnic ocean model. Part I: the subpolar gyre and high-latitude processes. J. Phys. Oceanogr. 26 (8), 1495–1527. http://dx.doi.org/10.1175/1520-0485(1996)026<1495:AIOABT>2.0.CO;2.
Salmon, R., 1998. Lectures on Geophysical Fluid Dynamics. Oxford University.
Serra, N., Ambar, I., 2002. Eddy generation in the Mediterranean undercurrent. Deep Sea Res. Pt. II 49 (19), 4225–4243. http://dx.doi.org/10.1016/S0967-0645(02)00152-2.
Shchepetkin, A.F., McWilliams, J.C., 2005. The regional oceanic modeling system (ROMS): a split-explicit, free-surface, topography-following-coordinate oceanic model. Ocean Modell. 9 (4), 347–404. http://dx.doi.org/10.1016/j.ocemod.2004.08.002.
Smith, K.S., 2007. The geography of linear baroclinic instability in Earth's oceans. J. Mar. Res. 65, 655–683.
Solodoch, A., Stewart, A.L., McWilliams., J.C., 2016. Baroclinic instability of axially-symmetric flow over sloping bathymetry. J. Fluid Mech. 799, 265–296.
Spall, M.A., 2004. Boundary currents and watermass transformation in marginal seas. J. Phys. Oceanogr. 34 (5), 1197–1213. http://dx.doi.org/10.1175/1520-0485(2004)034<1197:BCAWTI>2.0.CO;2.
Spall, M.A., 2010. Dynamics of downwelling in an eddy-resolving convective basin. J. Phys. Oceanogr. 40 (10), 2341–2347. http://dx.doi.org/10.1175/2010JPO4465.1.
Stern, A., Nadeau, L., Holland, D., 2015. Instability and mixing of zonal jets along an idealized continental shelf break. J. Phys. Oceanogr. 45 (9), 2315–2338. http://dx.doi.org/10.1175/JPO-D-14-0213.1.
Stewart, A.L., Dellar, P.J., Johnson, E.R., 2011. Numerical simulation of wave propagation along a discontinuity in depth in a rotating annulus. Comput. Fluids 46, 442–447.
Stewart, A.L., Dellar, P.J., Johnson, E.R., 2014. Large-amplitude coastal shelf waves. In: von Larcher, T., Williams, P.D. (Eds.), Modeling Atmospheric and Oceanic Flows. Wiley, Hoboken, NJ, pp. 229–253. http://dx.doi.org/10.1002/9781118856024.ch12.
Stewart, A.L., Thompson, A.F., 2012. Sensitivity of the ocean's deep overturning circulation to easterly Antarctic winds. Geophys. Res. Lett. 39 (18), L18604. 10.1029/2012GL053099.
Stewart, A.L., Thompson, A.F., 2013. Connecting Antarctic cross-slope exchange with Southern Ocean overturning. J. Phys. Oceanogr. 43, 1453–1471.
Stewart, A.L., Thompson, A.F., 2015a. Eddy-mediated transport of warm Circumpolar Deep Water across the Antarctic shelf break. Geophys. Res. Lett. 42 (2), 432–440. http://dx.doi.org/10.1002/2014GL062281.
Stewart, A.L., Thompson, A.F., 2015b. The neutral density temporal residual mean overturning circulation. Ocean Modell. 90, 44–56.
Stewart, A.L., Thompson, A.F., 2016. Eddy generation and jet formation via dense water outflows across the Antarctic continental slope. J. Phys. Oceanogr. 46, 3729–3750.
Stewart, K.D., Hogg, A.M., Griffies, S.M., Heerdegen, A.P., Ward, M.L., Spence, P., England, M.H., 2017. Vertical resolution of baroclinic modes in global ocean models. Ocean Modell. 113, 50–65.
Thoma, M., Jenkins, A., Holland, D., Jacobs, S., 2008. Modelling Circumpolar Deep Water intrusions on the Amundsen Sea continental shelf, Antarctica. Geophys. Res. Lett 35 (18). http://dx.doi.org/10.1029/2008GL034939.
Thompson, A.F., 2010. Jet formation and evolution in baroclinic turbulence with simple topography. J. Phys. Oceanogr. 40, 257–278.
Thompson, A.F., Young, W.R., 2007. Two-layer baroclinic eddy heat fluxes: zonal flows and energy balance. J. Atmos. Sci. 64, 3214–3231.
Towns, J., Cockerill, T., Dahan, M., Foster, I., Gaither, K., Grimshaw, A., Hazlewood, V., Lathrop, S., Lifka, D., Peterson, G.D., Roskies, R., Scott, J.R., Wilkins-Diehr, N., 2014. XSEDE: accelerating scientific discovery. Comput. Sci. Eng. 16 (5), 62–74. http://dx.doi.org/10.1109/MCSE.2014.80.
Tulloch, R., Marshall, J., Hill, C., Smith, K.S., 2011. Scales, growth rates, and spectral fluxes of baroclinic instability in the ocean. J. Phys. Oceanogr. 41 (6), 1057–1076. http://dx.doi.org/10.1175/2011JPO4404.1.
Vallis, G.K., 2006. Atmospheric and Oceanic Fluid Dynamics. Cambridge University.
Vallis, G.K., Maltrud, M.E., 1993. Generation of mean flows and jets on a beta plane and over topography. J. Phys. Oceanogr. 23, 1346–1362.
Venaille, A., 2012. Bottom-trapped currents as statistical equilibrium states above topographic anomalies. J. Fluid Mech. 669, 500–510.
Venaille, A., Vallis, G.K., Griffies, S.M., 2012. The catalytic role of the beta effect in barotropization processes. J. Fluid Mech. 709, 490–515.
Visbeck, M., Marshall, J., Haine, T., Spall, M., 1997. Specification of eddy transfer coefficients in coarse-resolution ocean circulation models. J. Phys. Oceanor. 27, 381–402.
Warneford, E.S., Dellar, P.J., 2017. Super- and sub-rotating equatorial jets in shallow water models of Jovian atmospheres: Newtonian cooling versus Rayleigh friction. J. Fluid Mech. 822, 484–511.
Willebrand, J., Barnier, B., Böning, C., Dieterich, C., Killworth, P.D., Provost, C.L., Jia, Y., Molines, J., New, A.L., 2001. Circulation characteristics in three eddy-permitting models of the North Atlantic. Progr. Oceanogr. 48 (2–3), 123–161. http://dx.doi.org/10.1016/S0079-6611(01)00003-9.
Wolfe, C.L., 2014. Approximations to the ocean's residual circulation in arbitrary tracer coordinates. Ocean Modell. 75, 20–35. http://dx.doi.org/10.1016/j.ocemod.2013.12.004.
Wolfe, C.L., Cessi, P., 2009. Overturning circulation in an eddy-resolving model: the effect of the pole-to-pole temperature gradient. J. Phys. Oceanogr. 39 (1), 125–142. http://dx.doi.org/10.1175/2008JPO3991.1.
Zhai, X., Greatbatch, R.J., 2007. Wind work in a model of the northwest atlantic ocean. Geophys. Res. Lett. 34 (4). http://dx.doi.org/10.1029/2006GL028907.
Zhang, Y., Pedlosky, J., Flierl, G.R., 2011. Cross-shelf and out-of-bay transport driven by an open-ocean current. J. Phys. Oceanogr. 41 (11), 2168–2186. http://dx.doi.org/10.1175/JPO-D-11-08.1.
Zhang, Z., Wang, W., Qiu, B., 2014. Oceanic mass transport by mesoscale eddies. Science 345, 322–324.